LOW-TEMPERATURE NUCLEAR QUADRUPOLE RESONANCE STUDIES OF ANTIMONY AND APPLICATION TO THERMOMETRY

By

EDGAR B. GENIO

A DISSERTATION PRESENTED TO THE GRADUATE SCHOOL
OF THE UNIVERSITY OF FLORIDA IN PARTIAL FULFILLMENT
OF THE REQUIREMENTS FOR THE DEGREE OF
DOCTOR OF PHILOSOPHY

UNIVERSITY OF FLORIDA

1997

© Copyright 1997

by

Edgar B. Genio

To My Parents

ACKNOWLEDGMENTS

I would like to thank Prof. Neil Sullivan for allowing me to join his research group as well as for being an adviser. It has been a privilege for me to study under someone with that rare gift of having both theoretical and experimental abilities.

I would also like to thank Profs. Gary Ihas, with whom I collaborated in this research, E. Dwight Adams, David Tanner, Peter Hirschfeld, and Wallace Brey for agreeing to serve on my supervisory committee.

I also thank Profs. Mark Meisel and Yasumasa Takano and Drs. Jian-sheng Xia, Jing-wei Xu, Tien Lang, and Paul Moyland for discussions, and for advice and help in the Microkelvin Lab; Dr. Bohdan Andraka for help in the annealing of the sample; the Cryogenic Engineering group, Greg Labbe and Brian Lothrop; Larry Frederick, the low-temperature physics group's electronics expert; the members of the Department of Physics electronics group under Larry Phelps; the members of the machine shop under the direction of Bob Fowler; and the past and present members of Prof. Sullivan's research group, Drs. Jaha Hamida, Peter Andersen, Morgan Evans, Kiho Kim, and Subrahmanyam Pilla, for their help, discussions and encouragement. This work was supported in part by the National Science Foundation, Grant numbers DMR-9216785 and DMR-9623536, and was performed in the University of Florida Microkelvin Laboratory, established through NSF Grant DMR-8419207.

My heartfelt thanks go to my family and my friends, near and far, for their encouragement, love, and support.

TABLE OF CONTENTS

ACKNOWLEDGMENTS iv

ABSTRACT vii

CHAPTERS

1 NUCLEAR QUADRUPOLE RESONANCE THEORY 1

- 1.1 Quadrupolar Interactions 1
- 1.2 Sources of Line Broadening 6
- 1.3 Time Dependent Interactions 7
- 1.4 Nuclear Relaxation 9
- 1.5 Pulsed NQR and the Free Induction Decay 10

2 EXPERIMENTAL APPARATUS 15

- 2.1 Sample Preparation 15
- 2.2 Experimental Cell 15
- 2.3 Cryostat 20
- 2.4 Pulsed NQR Spectrometer 21

3 RELAXATION MEASUREMENTS 27

- 3.1 Introduction 27
- 3.2 Korringa Relaxation 27
- 3.3 Other Sources of Relaxation 30
- 3.4 Relaxation Time Measurements 31
- 3.5 Results 33

4 SPIN COUPLING OF Sb TO ^{3}He 37

- 4.1 Introduction 37
- 4.2 Bulk and Surface Relaxation Analysis 37
- 4.3 ^{3}He-mediated Surface Relaxation 40
- 4.4 Relaxation analysis of Sb coupled to liquid ^{3}He 42
- 4.5 Sb-^{3}He coupling model 46
- 4.6 Conclusion 46

5 POPULATION DIFFERENCE THERMOMETRY 51

5.1 Introduction 51
5.2 Principles 51
5.3 Magnetic Field Perturbed NQR 53
5.4 Experimental Apparatus 63
5.5 Results 64
5.6 Discussion and Conclusion 65

APPENDICES

A QUENCH CONTROL CIRCUIT 70

B FAST AMPLIFIER 72

REFERENCES 74

BIOGRAPHICAL SKETCH 77

Abstract of Dissertation Presented to the Graduate School
of the University of Florida in Partial Fulfillment
of the Requirements for the Degree of
Doctor of Philosophy

LOW-TEMPERATURE NUCLEAR QUADRUPOLE RESONANCE STUDIES OF ANTIMONY AND APPLICATION TO THERMOMETRY

By

Edgar B. Genio

May 1997

Chairman: Neil S. Sullivan
Major Department: Physics

The spin-lattice relaxation time, T_1 , of finely divided powdered metallic antimony immersed in liquid ^{3}He was measured using pulsed Nuclear Quadrupole Resonance (NQR) techniques. In this technique, the nuclear quadrupole resonant antimony nuclei were saturated using an RF pulse. The recovery back to equilibrium was monitored using short inspection pulses and the magnetization recovery follows a recovery curve charaterized by the relaxation time T_1 .

T_1 measurements were performed at temperatures ranging from 150 mK to 1.25 mK. Temperatures down to 11 mK were achieved by using a dilution refrigerator. Lower temperatures were achieved using adiabatic nuclear demagnetization of a copper bundle starting at 8.5 Tesla (7.5 Tesla average field over the copper bundle). The sample was cooled by immersion in liquid ^{3}He which is in thermal contact with silver sinter packed in the bottom of a silver cell. This cell was bolted onto a cold plate attached to the copper bundle.

It was found that at low temperatures starting near 75 mK, the measured total relaxation was significantly enhanced with respect to the Korringa relaxation, the dominant relaxation mechanism expected for a metal at these temperatures. This enhancement is attributed to a surface relaxation mechanism mediated by the surface ^{3}He atoms.

In systems immersed in liquid ^{3}He , a surface relaxation mechanism is present due to a modulation of the interaction between the solid-like ^{3}He atoms on the surface and the surface spins. This modulation is due to the quantum zero-point motion of the ^{3}He atoms on the surface. This phenomenon has been well studied in insulating systems using Nuclear Magnetic Resonance.

The measurements undertaken in this study demonstrate that this phenomenon is present in a metallic and quadrupolar system. This surface relaxation mechanism becomes the dominant relaxation mechanism at low temperatures. Considering the surface and bulk spins as belonging to different phases, a two phase relaxation analysis was used to extract the surface relaxation parameters. This work helps explain previous relaxation measurements by other groups, on powdered metals (with spin $I \neq 0$) immersed in liquid ^{3}He . In these studies, anomalies were reported whose features are consistent with the surface relaxation mechanism discussed in this work.

Using magnetic field perturbed NQR, the intensity ratio of two transitions was studied from 1.4 mK to 0.25 mK. The intensity ratio was observed to change as a function of temperature. A comparison is made with the expected Boltzmann distribution. This intensity ratio can be used as a self-calibrating, absolute thermometer for the ultra-low temperature region.

CHAPTER 1
NUCLEAR QUADRUPOLE RESONANCE THEORY

1.1 Quadrupolar Interactions

In addition to spin, some nuclei have a quadrupole moment Q. If these nuclei are in an environment where there is an electric field gradient (EFG) produced by charges external to the nucleus, there will be an interaction between the nucleus and this EFG. The components of this EFG can be expressed as

$$V_{ij} = \frac{\partial^2 V}{\partial x_i \partial x_j}. \tag{1.1}$$

V_{ij} is symmetric and since the charges are external to the nucleus, $\nabla^2 V = 0$ at the location of the nucleus. These conditions reduce the number of independent components of V_{ij} to 5. Choosing a coordinate system $\{x, y, z\}$ so that the off-diagonal elements vanish, the principal components of this EFG become V_{xx}, V_{yy}, and V_{zz}. With the condition

$$V_{xx} + V_{yy} + V_{zz} = 0, \tag{1.2}$$

only two parameters are needed to specify the EFG. One can choose the z axis to coincide with the direction of maximum gradient and the x direction along the minimum gradient, that is

$$|V_{zz}| \geq |V_{yy}| \geq |V_{xx}|. \tag{1.3}$$

With this choice of axis, one can choose the two parameters defining the EFG to be eq and η defined by

$$\begin{aligned} eq &= V_{zz}|_{r=0} && (1.4) \\ \eta &= \left|\frac{(V_{xx} - V_{yy})}{V_{zz}}\right|. && (1.5) \end{aligned}$$

Because of its definition, η is known as the asymmetry parameter and $\eta = 0$ for an axially symmetric EFG. Such is the case for an EFG which is spherically symmetric or if it has cubic symmetry for which case $V_{xx} = V_{yy} = V_{zz}$ and application of eqn. 1.2 makes all these components vanish. Therefore, there is no quadrupolar interaction for nuclei in a cubic lattice. The symmetry of the crystal is very much reflected in the symmetry of the EFG [1]. Crystal symmetries with n-fold rotation or rotation-reflection with $n > 2$ gives $\eta = 0$. If there are two or more of such axes, the EFG vanishes as was the case for cubic symmetry. In what follows, we consider only axially symmetric EFGs, that is, the V_{xx} and V_{yy} components of the EFG are equal. This is the case applicable to the system being studied here.

The discussion of quadrupolar interaction in this section follows that of Das and Hahn [2]. Consider a quadrupole moment bearing nucleus in an axially symmetric electric field gradient (EFG) provided by the electronic charge distribution in the lattice (shown schematically in Fig. 1.1). The classical quadrupolar interaction is given by

$$W_Q = \frac{1}{4}\frac{\partial^2 V}{\partial z'^2}\int \rho_N(3z'^2 - r^2)dV \tag{1.6}$$

where ρ_N is the nuclear charge distribution.

Evaluated in the symmetry axis frame,

$$W_Q = \frac{1}{4}eQ\frac{\partial^2 V}{\partial z^2}(\frac{3}{2}cos^2\theta - \frac{1}{2}) \tag{1.7}$$

where

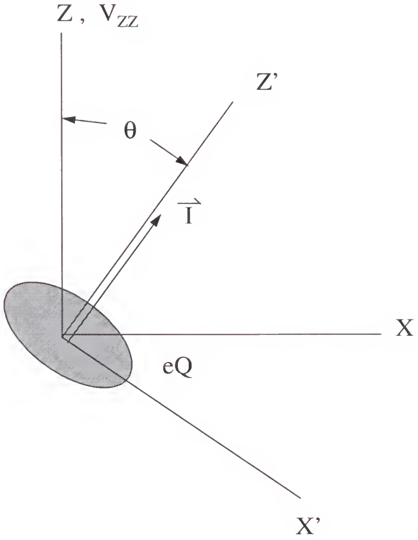

Figure 1.1: Orientation of the nucleus: the unprimed axes are fixed in space and the primed axes are local to the nucleus represented by the ellipsoid.

$$eQ = \int \rho_N (3z^2 - r^2) dV. \tag{1.8}$$

Q is the quadrupole moment evaluated completely aligned to some symmetry axis. It can be seen from Eq. 1.7 that W_Q is orientation dependent.

In the quantum mechanical treatment, the orientation is quantized by replacing $cos^2 \theta$ with $I_z^2/I(I+1)$. The quadrupole moment is Q_I evaluated about the I-axis when considered as the symmetry axis. Q_I is related to the observed Q through [3]

$$Q = \frac{I - \frac{1}{2}}{I+1} Q_I. \tag{1.9}$$

Note that the measured quadrupole moment Q vanishes for $I = \frac{1}{2}$.

Putting these into Eq. 1.7, the energies are

$$E_m = \frac{1}{8} e^2 q Q_I \left\{ \frac{3m^2 - I(I+1)}{I(I+1)} \right\} \tag{1.10}$$

or in standard notation,

$$E_m = \frac{e^2 qQ}{4I(2I-1)} [3m^2 - I(I+1)]. \tag{1.11}$$

This result holds for both half-integral and integral spins. For half-integral spins, there are $I + \frac{1}{2}$ energy levels, each one doubly degenerate in m as states with $\pm m$ have the same energy. For integral spins, there are $I + 1$ energy levels, each one doubly degenerate except for the $m = 0$ state.

Because of this orientation dependence, the quadrupole precesses about the z-axis defined by the maximum field gradient. This means that there are rotating components associated with the magnetic dipole moment $\boldsymbol{\mu}$. The $+m$ and $-m$ states have the same energy and precess with the same frequency. However, they precess in opposite directions.

An RF magnetic field $\boldsymbol{H}(t)$ which interacts with the magnetic dipole moment of the nucleus can induce transitions between these energy levels. This interaction is given by

$$V = -\boldsymbol{\mu} \cdot \boldsymbol{H}(t). \tag{1.12}$$

In cartesian form,

$$V = -\gamma\hbar[H_x(t)I_x + H_y(t)I_y + H_z(t)I_z]. \tag{1.13}$$

Here, γ is the nuclear gyromagnetic ratio, and $H_x(t), H_y(t), H_z(t)$ are the components of the linearly polarized RF magnetic field $2H_1 cos\, \omega t$. I_x, I_y, I_z are the angular momentum operators.

The matrix elements for the angular momentum operators are

$$\begin{aligned} \langle m|I_z|m'\rangle &= m\delta_{mm'} \\ \langle m|I_x \pm iI_y|m'\rangle &= \sqrt{(I \pm m)(I \mp m + 1)}\delta_{m\mp1,m'}. \end{aligned} \tag{1.14}$$

As can be seen from these matrix elements and the interaction given by Eq. 1.13, transitions $\Delta m = \pm 1$ are induced only by the perpendicular components of the RF field relative to the symmetry axis of the electric field gradient (which defines the z direction). Thus for an arbitrarily oriented $\boldsymbol{H}(t)$, only the perpendicular component $H(t) sin\, \theta$ is effective where θ is the angle between the symmetry axis and $\boldsymbol{H}(t)$.

The transition probability W is given by

$$W \sim |\langle i|V|f\rangle|^2. \tag{1.15}$$

W involves the square of the matrix elements given in Eq. 1.14 and the intensity of the transition will have the angular dependence $sin^2\theta$ due to the orientation of the RF coil which generates $\boldsymbol{H}(t)$.

The frequency of transition between energy levels $m+1$ and m is given by

$$\omega_m = \frac{(E_{m+1} - E_m)}{\hbar}. \tag{1.16}$$

Using Eq. 1.11, these transition frequencies are

$$\omega_m = \frac{3A}{\hbar}(2|m| + 1) \tag{1.17}$$

where $A = \frac{e^2qQ}{4I(2I-1)}$. It can be seen that the energy level differences are unequal.

The transition frequencies for antimony, the system under study, have been found experimentally using continuous wave NQR and reported by Hewitt and Williams [8]. For antimony, the unit cell is of the trigonal arsenic-type structure and the EFG is axially symmetric ($\eta = 0$) as expected from the symmetry of its crystal structure [8].

Table 1.1: NQR transition frequencies and coupling constants for Sb.

Nucleus	Transition	Frequency (MHz)	A	e^2qQ
^{121}Sb	$(\frac{3}{2} - \frac{1}{2})$	11.5289	1.922 MHz $\times 2\pi\hbar$	76.867 MHz $\times 2\pi\hbar$
	$(\frac{5}{2} - \frac{3}{2})$	23.0611		
^{123}Sb	$(\frac{3}{2} - \frac{1}{2})$	6.9996	1.166 MHz $\times 2\pi\hbar$	98.0 MHz $\times 2\pi\hbar$
	$(\frac{5}{2} - \frac{3}{2})$	13.9997		
	$(\frac{7}{2} - \frac{5}{2})$	21.0000		

From these measured transition frequencies, the coupling constants can be obtained. The transition frequencies and the coupling constants are shown in Table 1.1.

1.2 Sources of Line Broadening

Some sources of line broadening are briefly summarized in this section. One source of broadening is the imperfections in the crystal lattice which include strains, structural defects or low level impurities. All these lead to an EFG which varies from site to site. Since the nuclear quadrupole moment interacts with the electric field gradient (EFG) created by the electronic charge distribution, which depends on the lattice geometry, this inhomogeneity in the EFGs slightly shifts the resonant frequency of the nuclei resulting in a broadening of the line.

Another source of broadening is the dipole-dipole interaction between the nuclei in a rigid lattice. Each of the neighboring dipoles can introduce a splitting of the NQR line. The superposition of these splittings from different neighbors gives a smeared out NQR line.

If there is internal motion, a non-vanishing zero frequency component or non-zero $< H_z^2 >_{ave}$ generated by the movement of the other dipoles at the site of the nucleus cause small zeeman splittings, leading to a broadening of the NQR absorption line.

1.3 Time Dependent Interactions

In this section, the effects of time dependent interactions are briefly discussed. For these effects, there are two time scales defined by some characteristic time τ. For the long time scale, $t >> \tau$, while for the short time scale, $t \leq \tau$. These time dependent fluctuations can be resolved into a frequency spectrum $S(\omega)$. An example of such a spectrum is shown in Fig. 1.2.

The DC to low frequency components of the spectrum contribute to a broadening of the line (T_2 effect). If the spectrum contains frequency components which hit a frequency resonance (allowing energy exchange), it affects the spin-lattice relaxation (T_1 effect). In Fig. 1.2 for example, nucleus ***b*** does not experience relaxation while nucleus ***a*** does. An example of this is the time dependent EFG fluctuations. It is the source of the electric contribution to the total relaxation, W_Q.

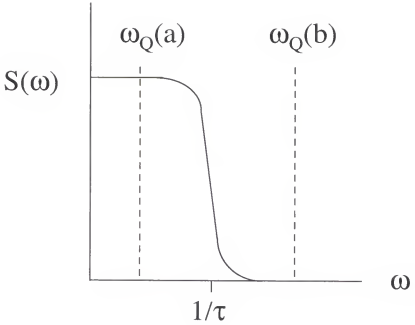

Figure 1.2: A model frequency spectrum of time dependent fluctuations. τ is the characteristic time.

1.4 Nuclear Relaxation

In this subsection, the relaxation of the system back to equilibrium is briefly discussed and follows the procedure developed by MacLaughlin *et al.* [4]. For magnetic relaxation ($\Delta m = 1$), the transition probability is given by

$$W_{mn} = \frac{2\pi}{\hbar} \left|\langle m|\boldsymbol{\mu} \cdot \boldsymbol{H}_e|n\rangle\right|^2 \delta(E - E') \tag{1.18}$$

Using Eq. 1.14 for the matrix elements,

$$W_{mn} = W[(I \mp m)(I \pm m + 1)] \tag{1.19}$$

where W includes all the prefactors.

The rate equation governing relaxation is

$$\frac{dP_m}{dt} = \sum_{n=-I}^{I} W_{mn}(P_n - P_m) \tag{1.20}$$

where P_m is the deviation from equilibrium population. In terms of the population differences U_m (symmetrized to account for the degeneracy of the $\pm m$ states),

$$U_m = (P_m - P_{m-1}) + (P_{-m} - P_{-m+1}), \tag{1.21}$$

the rate equation given by Eq. 1.20 becomes the matrix equation

$$\frac{d\boldsymbol{U}}{dt} = -\underline{A}\,\boldsymbol{U} \tag{1.22}$$

where $\underline{A}$ is the relaxation matrix. The formal solution is

$$\boldsymbol{U}(t) = e^{-\underline{A}t}\,\boldsymbol{U}(0). \tag{1.23}$$

Written explicitly in terms of its components,

$$U_m(t) = \sum_i \alpha_{mi}\, a_i\, exp(-\lambda_i t) \tag{1.24}$$

where λ_i are the $I - \frac{1}{2}$ non-degenerate eigenvalues of the relaxation matrix $\underline{A}$, α_{mi} are the components of the corresponding eigenvectors and a_i are the initial conditions. For NQR, due to the inequality of the energy level differences, the relaxation is in general multi-exponential: single exponential for nuclei with $I = \frac{3}{2}$, double exponential for $I = \frac{5}{2}$, etc. For a spin $I = \frac{5}{2}$ nucleus, the complete solution to the relaxation equation is given by [4]

$$\begin{aligned} U_{(\frac{5}{2}-\frac{3}{2})}(t) &= A_{(\frac{5}{2}-\frac{3}{2})}(0.429\, exp(-6W_m t) + 0.571\, exp(-20W_m t)) && (1.25) \\ U_{(\frac{3}{2}-\frac{1}{2})}(t) &= A_{(\frac{3}{2}-\frac{1}{2})}(0.107\, exp(-6W_m t) + 0.893\, exp(-20W_m t)) && (1.26) \end{aligned}$$

where $W_m = 1/2T_1$ is the magnetic ($\Delta m = 1$) relaxation rate. It is also seen from these solutions that the relaxation involves time constants which are fractions of T_1.

1.5 Pulsed NQR and the Free Induction Decay

The response of a quadrupolar system to a pulsed RF magnetic field has been treated by Bloom, Hahn and Herzog [5], Das and Saha [6] and a brief discussion is also found in Das and Hahn [2]. In their quantum mechanical treatment, the time dependent Schrödinger equation is solved for the case where an RF magnetic field at the resonant frequency is on only during a short period of time t_w. During this time, the system is driven and evolves according to a Hamiltonian which includes both the quadrupolar interaction and the magnetic coupling to the RF field. At times $t > t_w$, when the RF field is off, the system decays under the quadrupolar Hamiltonian alone. This decay of the RF magnetization, which is the experimentally observed quantity is called the "Free Induction Decay" or FID.

Suppose that the RF magnetic field is applied perpendicular to the symmetry axis at the resonant frequency ω_o and with an amplitude H_1. Choosing the x-axis for the direction of the RF coil, the RF magnetic field $\boldsymbol{H}(t)$ has components $H_x(t) = 2H_1 \cos \omega t$, $H_y(t) = H_z(t) = 0$.

The Hamiltonian governing the evolution of the system is

$$H = \begin{cases} H_Q + H_m & 0 < t < t_w \\ H_Q & t > t_w \end{cases} \tag{1.27}$$

where

$$H_Q = \frac{e^2 q Q}{4I(2I-1)}(3I_z^2 - I^2) \tag{1.28}$$

and

$$H_m = -\gamma \hbar \boldsymbol{I} \cdot \boldsymbol{H}(t). \tag{1.29}$$

For times $t > t_w$, the nuclear spins precess freely under the influence of the quadrupolar Hamiltonian H_Q alone.

In the following derivation, the case $I = \frac{3}{2}$ is considered and at the end, the result is generalized to an arbitrary spin I. The wavefunction ψ of the nuclear spin can be written as

$$\psi = \sum_{m=-\frac{3}{2}}^{\frac{3}{2}} C_m(t)\, \psi_m\, e^{iE_m t/\hbar} \tag{1.30}$$

where ψ_m are the eigenstates of the quadrupolar Hamiltonian H_Q, and E_m are the energies. The time evolution of the system is completely determined by the coefficients $C_m(t)$ since the stationary solutions ψ_m are known.

For times $0 < t < t_w$, the time dependent Schrödinger equation is

$$i\hbar \frac{d\psi}{dt} = (H_Q + H_m)\psi. \tag{1.31}$$

After the pulse, the Schrödinger equation becomes

$$i\hbar \frac{d\psi}{dt} = H_Q \psi. \tag{1.32}$$

Using Eq. 1.30 into the Schrödinger equation given by Eq. 1.32, the evolution of the wavefunction after some arbitrary time t_o is

$$\psi(t+t_o) = \sum_{m=-\frac{3}{2}}^{\frac{3}{2}} C_m(t_o)\,\psi_m\, e^{iE_m t/\hbar}. \tag{1.33}$$

The time dependence only comes from the time dependence of the stationary states and the coefficients are determined by the initial conditions and do not change with time.

For the case when H_m is present, the solution to the Schrödinger equation after some arbitrary time t_o is

$$\psi(t+t_o) = \sum_{m=-\frac{3}{2}}^{\frac{3}{2}} C_m(t+t_o)\,\psi_m\, e^{iE_m t/\hbar}. \tag{1.34}$$

The two sets of coefficients are related through a matrix equation

$$C_m(t+t_o) = R\, C_m(t_o) \tag{1.35}$$

where the matrix R is

$$R = \begin{vmatrix} cos\frac{\sqrt{3}\omega_1 t}{2} & 0 & isin\frac{\sqrt{3}\omega_1 t}{2} & 0 \\ 0 & cos\frac{\sqrt{3}\omega_1 t}{2} & 0 & isin\frac{\sqrt{3}\omega_1 t}{2} \\ isin\frac{\sqrt{3}\omega_1 t}{2} & 0 & cos\frac{\sqrt{3}\omega_1 t}{2} & 0 \\ 0 & isin\frac{\sqrt{3}\omega_1 t}{2} & 0 & cos\frac{\sqrt{3}\omega_1 t}{2} \end{vmatrix}. \tag{1.36}$$

In the expression for R, $\omega_1 = \gamma H_1$ where $2H_1$ is the amplitude of the RF magnetic field.

The solution of the Schrödinger equation for times $t > t_w$ is

$$\psi = \sum_{m=-\frac{3}{2}}^{\frac{3}{2}} C_m(t_w)\,\psi_m\, e^{iE_m(t-t_w)/\hbar}. \tag{1.37}$$

$C_m(t_w)$ are the "initial conditions" for $t > t_w$ and are obtained from the coefficients at $t = 0$ through the rotation matrix R.

Using the solution given by Eq. 1.37, the expectation values of the angular momentum operators can be evaluated and the results are

$$\langle I_x\rangle = \frac{\sqrt{3}}{2}\, sin\sqrt{3}\omega_1 t_w\; sin\omega_o(t - t_w) \tag{1.38}$$

$$\langle I_y\rangle = 0 \tag{1.39}$$

$$\langle I_z\rangle = 0. \tag{1.40}$$

The quantity $\sqrt{3}\omega_1 t_w$ represents the angle through which the magnetization vector is rotated by H_1 and ω_o is the resonant frequency. From these solutions, it is seen that the magnetization is linearly polarized.

The line broadening can be taken into account by introducing the gaussian function

$$g(\omega_o' - \omega_o) = \frac{1}{\delta\sqrt{2\pi}} exp\left\{\frac{-(\omega_o' - \omega_o)^2}{2\delta^2}\right\} \tag{1.41}$$

where δ is the root-mean square frequency width of the line. After averging over this gaussian distribution, Eq. 1.38 becomes

$$\langle I_x\rangle = \frac{\sqrt{3}}{2}\, sin\sqrt{3}\omega_1 t_w\; sin\omega_o(t - t_w)\, exp\left\{\frac{-\delta^2(t - t_w)^2}{2}\right\}. \tag{1.42}$$

This is the free induction decay (FID) whose envelop decays according to the broadening of the absorption line. In the experiments, it is this envelop that is detected by the detection system. It is also seen from Eq. 1.42 that the amplitude of the FID is maximum when $\sqrt{3}\omega_1 t_w = \frac{\pi}{2}$. For this condition, the pulse width t_w corresponds to a 90° pulse. From this condition of maximum amplitude, the strength of the RF field can be estimated using $\omega_1 = \gamma H_1$. The generalization to an arbitrary spin I is done by replacing the factor $\sqrt{3}$ by $\sqrt{(I - |m|)(I + |m| + 1)}$.

As a note on the experimental arrangement: since there is no magnetization along the y-axis according to Eq. 1.39, a cross-coil arrangement (where the excitation coil is in the x-direction and the detection coil in the y-direction) cannot work for pure quadrupole resonance. However, cross-coil experiments are possible for magnetic field perturbed NQR where the degeneracy in $\pm m$ is lifted.

CHAPTER 2
EXPERIMENTAL APPARATUS

2.1 Sample Preparation

High purity (99.9999%) antimony shot [7] was crushed into a fine powder using a mortar and pestle and sieved to less than 25 μm. The resulting powder was placed in a quartz tube which was evacuated and sealed. The sample was then carefully annealed at 550° C for 4 hrs. following the procedure prescribed by Hewitt and Williams [8]. To remove the grains which formed sintered agglomerates, the annealed powder was sieved again. This annealing process reduces lattice inhomogeneities. This would lead to an additional broadening of the NQR line due to variations in the local electric field gradients as discussed in chapter 1. The finely divided, annealed powder was mixed with fine silica powder of the same grain size. The mixture ratio was below the percolation limit (15% antimony by volume) to reduce inter-grain conduction and RF heating of the metallic sample during the applied RF pulses.

2.2 Experimental Cell

The sample cell was a jelly-roll tower made of Kapton [9] and Stycast 1266 [10] epoxy. The tower consisted of 4 layers of Kapton sheet rolled into a cylinder with the epoxy applied in between the layers. To prevent unwinding, the cylinder was clamped by a wooden clothespin and was left to cure overnight. After it cured, the extra Kapton was trimmed and the tube was cut to the desired length using a sharp scalpel. Stycast was used to close off one end of the tower.

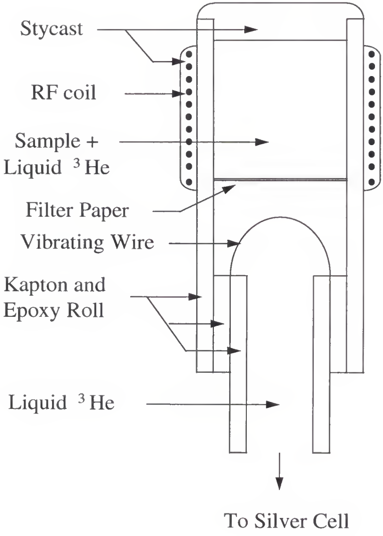

Figure 2.1: Tower with sample and RF coil.

The loosely packed powder mixture was situated at the closed end of the tube and held by filter paper [11] (1.2 μm holes) which allowed the liquid ^{3}He ($<$ 10 ppm impurities) to flow into the sample. The powder mixture occupied a volume of about 0.1 cc. Estimating the packing fraction to be 50% and with the mixture being 15% Sb, the total Sb sample was about 16 mg ($\approx$ 42 mmoles). It is important to have the least amount of the sample possible to keep the total heat capacity very small to be able to cool it efficiently. Additionally, because the sample is in a powder form, the surface area is very large. These two considerations allow the sample to quickly reach equilibrium with the liquid ^{3}He . The tower and RF coil are shown in Fig. 2.1.

The open end of the tube was epoxied to a silver housing using Stycast 2850. This silver housing contains the silver sinter heat exchanger, with about 29 m^2 of surface area. The silver housing was bolted onto the cold plate to which the 330 mole copper stage of an adiabatic demagnetization refrigerator is attached. The same silver housing contains an ultrasound transmitter and receiver used for sound attenuation studies in the liquid ^{3}He [12].

A small superconducting magnet surrounding the sample area was used for non-zero field studies. This magnet has 10 layers (104 turns per layer) of superconducting wire with, the first layer having a 30-turn notch (1 layer without the middle 30 turns) to extend the homogeneity of the magnetic field. The uniformity of the magnetic field is about 0.7 percent over 0.27 inches about the center. These values are according to the results of the magnet design parameters.

In making the magnet, GE varnish diluted with acetone was applied to each completed layer to fix it in position. The magnet former is copper with a vertical cut to interrupt the conduction path to reduce eddy current heating. This gap was filled with Stycast 2850 to restore structural stability to the former. The magnet was supported by vespel rods which thread into the top flange of the silver housing. Vespel provides high thermal isolation of the silver cell from the magnet assembly which is anchored to the mixing chamber of the dilution refrigerator. A superconducting shield made of lead sheet screened out the whole assembly from fringe external fields. The complete assembly is shown in Fig. 2.2.

The RF coil used for NQR measurements was wound around the sample tube and fixed using Stycast 1266. This coil, about 0.2" in diameter and 0.275" in length consisted of 11 turns of copper wire and had an inductance of about 0.7 μH. The sample coil was centered around the homogeneous region of the magnet. The same coil is used for the excitation of the sample and the reception of the NQR signals.

A home-made coaxial cable connected the RF coil to an existing commercial coaxial cable running halfway down from the top of the cryostat. This home-made cable had a superconducting NbTi center wire and the outer conductor is CuNi, 30 mils in outer diameter. The space between conductors was filled with Apiezon N [13] grease for stability of the inner conductor as well as for thermal contact. The ends of this coaxial cable were sealed with Stycast 1266 for vacuum sealing. A suitable length of additional coaxial cable, adjusted so that the total length was $\lambda/2$, completed the connection to the duplexer box of the spectrometer on top of the cryostat.

Due to the small amount of sample used (in favor of efficient thermal contact and quick thermal times), a concern about the signal detection arose. To find out the size of the signals, a tower was constructed similar in all respects to the actual tower used. The same amount of sample mixture was used and the same RF coil was wound around the sample end of the tower. The filter paper used to hold the powder mixture at one end of the tower was pierced by several copper wires covered with Apiezon N grease. The ends of these copper wires were twisted together and screwed onto a cold plate attached to the bottom plate of the mixing chamber of a dilution refrigerator, located in Rm 141 Williamson Hall. These copper wires formed the thermal link to the sample. Satisfactory signal sizes were observed and relaxation measurements were conducted as practice runs.

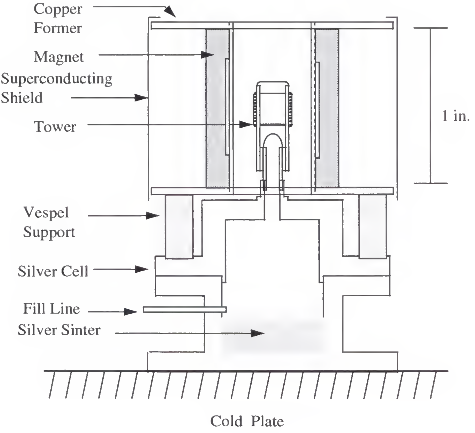

Figure 2.2: Complete experimental assembly showing the tower, magnet, and silver housing.

2.3 Cryostat

The experiments described in this dissertation were performed in the second bay cryostat at the University of Florida Microkelvin Research Laboratory. This laboratory was constructed through a grant fron the National Science Foundation with support from the University of Florida and the State of Florida. This facility is the largest ultra-low temperature laboratory in the world and is one of only two ultra-low temperature laboratories in the United States, the other one being at Cornell University.

There are three bays in this laboratory, each with a 15-foot dewar supported by 23-foot concrete tripods. These tripods are anchored in 5-ton concrete blocks independent of the building for mechanical isolation from ambient vibrations. At the top of these concrete tripods are three active air isolation mounts which support a tri-layer aluminum triangular plate. The dewar is suspended from this aluminum plate. A welded steel and copper shielded room surrounds the area around the top of the cryostat. A welded aluminum cylinder surrounds the dewar and connects to the shielded room. This shielded room and cylinder combination screens out electromagnetic interferences. More detailed information about this cryostat and the facilities at the Florida Microkelvin Laboratory can be found in references [14, 15, 16].

The experimental assembly was bolted to a cold plate which formed the bottom part of a copper 'cage'. This cage consists of two copper plates connected by copper pillars. Low temperature experiments are mounted on the bottom plate as well as on the top plate. This copper cage is connected to an Oxford dilution refrigerator [17] through an aluminum superconducting heat switch. With the heat switch closed, the dilution refrigerator cools the entire assembly down to 10 mK.

To achieve lower temperatures, an adiabatic nuclear demagnetization refrigerator was used. This refrigerator consisted of a 330-mole copper nuclear demagnetization bundle. A two stage cooling was used. With the heat switch closed, the dilution refrigerator pre cooled the cage and the bundle with the bundle in an 8.5 Tesla magnetic field (peak). The average field over the length of the bundle was about 7.5 Tesla. Upon reaching 12 mK, the heat switch was opened to thermally isolate the cage and the bundle. Decreasing the magnetic field (adiabatic nuclear demagnetization) cools the bundle by cooling the nuclear spins. The electronic temperature is lowered through the electron-nuclei coupling. Using these procedures, temperatures in the microkelvin range can be achieved.

The superconducting magnet used for demagnetization was powered by a Cryomagnetics 100A Power Supply programmed by a ramp controller. This power supply was used for currents down to 10A. A Kepco Power Supply was used for demagnetization using currents below 10A with the ramp controller reset to its maximum value. This provides a finer resolution when in the low current stage of the demagnetization.

2.4 Pulsed NQR Spectrometer

Pulsed NQR spectroscopy is a Fourier Transform spectroscopy where the excitation contains a wide band of frequencies and the resulting signal contains the frequency information (the spectrum) in the time domain. A Fourier transformation is required to recover the spectrum. For the excitation to contain a wide range of frequencies about a central RF frequency, an intense RF pulse is used. The resulting signal, the Free Induction Decay (FID) is very weak and is detected by a low-noise, high-sensitivity RF amplifier.

The block diagram for the pulsed NQR spectrometer is shown in Fig. 2.3. To generate the RF pulse, a signal generator provides continuous RF to a mixer used as a 'gate'. This gate highly attenuates the RF when the control voltage is 0 V and lets the RF pass when the control voltage is around 5V. An RF pulse is generated when a 5 V pulse with the desired pulse width is applied as the control voltage. Two such

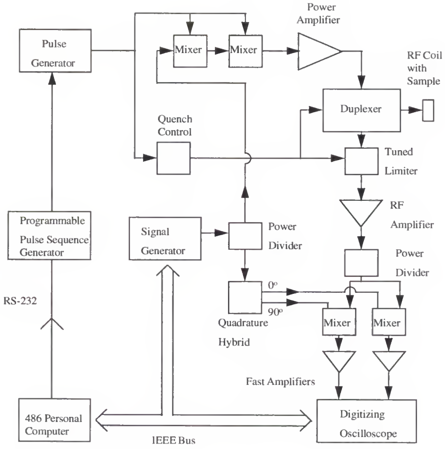

Signal Generator: HP 8656B
Pulse Generator: Wavetek 859
Digitizing Oscilloscope: Tektronix 2230

Figure 2.3: Block diagram of the pulsed NQR spectrometer.

mixers are used in series to provide a very high ON/OFF ratio. The control pulses come from the Pulse Generator with the pulse widths determined by a computer controlled pulse sequence generator.

The FID immediately follows the RF excitation pulse and is very short in duration. There must be a means of applying the RF pulse to the sample without overwhelming the pre-amplifier, which needs to recover quickly from the overload to receive the FID. This switching between the excitation mode and the reception mode without interfering with each other is done by using a duplexer (see Fig. 2.4).

Two important components in the duplexer are the crossed diodes CD and the diode rings DR. The crossed diodes look like a short to a large voltage (greater than 0.5 V, the typical diode voltage drop) and for very small voltages, they look like open circuits. This passive discrimination between large voltages and small voltages is put to use in switching between the excitation mode (with the large RF excitation) and the signal reception mode, where the weak FID signal immediately follows the RF excitation pulse. The diode rings function in a similar way except that it is actively controlled by the quench control circuit (described in Appendix A) using control pulses which extend the cut-off voltages of the diodes.

During the large RF excitation, all the crossed diodes and the diode rings are seen as short circuits. The RF excitation is capacitively coupled using C_0 and goes to the resonant tank circuit formed by the inductors L_s, L_1 and the capacitors C_1 and C_T. The Q of this tank circuit was about 12. During the excitation, the pre-amplifier is isolated. After the RF pulse, when the ringdown from the transmitter has reached a level where it is cut off by the diodes, the crossed diodes and the diode rings act like open circuits. This isolates the transmitter from the duplexer, and the FID is picked up by the tuned resonant tank circuit formed by L_s and C_T. This FID signal proceeds to the pre-amplifier through the series resonant L_1, L_2 and C_2 which act like a short to the FID. Additional isolation is provided by the tuned limiter immediately

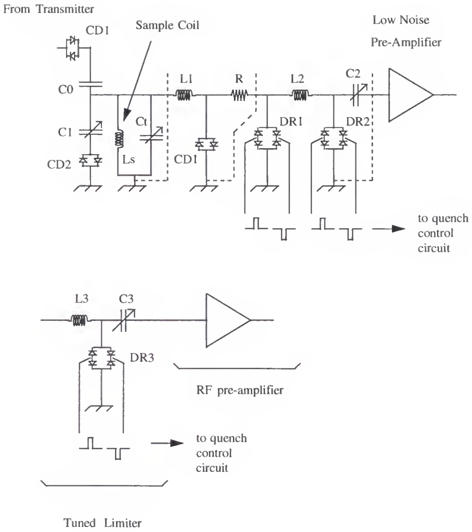

Figure 2.4: Circuit diagram for the duplexer and tuned limiter.

after the pre-amplifier. This tuned limiter provides an active quench control using a diode ring in addition to the natural frequency selectivity of the series resonant circuit provided by L_3 and C_3.

After another amplifier, the signal is split and quadrature detected. Quadrature detection is obtained by mixing the signal with continuous RF derived from the signal generator through a quadrature hybrid, one with 0° and the other with 90° phase difference. The output of these mixers form in-phase and quadrature components of the FID and are amplified by ultra-fast amplifiers (see Appendix B). These are digitized and stored by the digitizing oscilloscope and transferred to the computer over the IEEE Bus. A fiber optic IEEE cable connected the instruments inside the shielded room to the outside where the computer was located.

Shown in Fig. 2.5 is a single shot FID signal at 3 mK following a 1.5 μs RF pulse at 11.5289 MHz, the frequency of the $\pm\frac{3}{2}$ to $\pm\frac{1}{2}$ transition . The corresponding linewidth is about 25 kHz primarily due to nuclear dipole interactions. At this frequency, the anomalous skin depth was about 1 μm.

Higher temperatures were monitored using a ^{3}He melting curve thermometer (MCT) calibrated against the superfluid “A” and Neel transition of solid ^{3}He. In this form of thermometry, the melting pressure of ^{3}He is monitored by a Straty-Adams capacitive pressure strain gauge [18, 19], calibrated against a precision Paroscientific pressure gauge [20]. The melting pressure is a unique function of temperature below 319 mK, the temperature at which the melting pressure is minimum.

A ^{195}Pt NMR thermometer operating at 125 kHz was used below 1 mK. For ^{195}Pt, the ordering temperature is estimated to be a few microkelvins or lower and so the nuclear susceptibility obeys Curie law at the operating temperatures considered here. This behavior can be used to extrapolate the temperature after calibration against the MCT at high temperatures. In addition, the magnitude of the FIDs also gave us a reliable indication of the sample temperature.

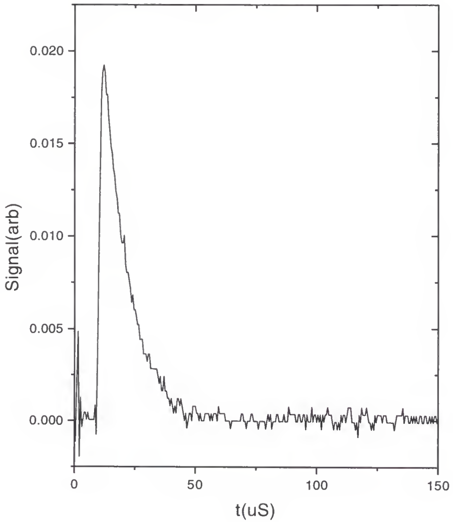

Figure 2.5: Free induction decay following a single 1.5 μs RF pulse at 3 mK.

CHAPTER 3
RELAXATION MEASUREMENTS

3.1 Introduction

In this chapter, nuclear spin-lattice relaxation measurements on ^{121}Sb (I=$\frac{5}{2}$, $\frac{\gamma}{2\pi}$ = 1.02 kHz/gauss, 57% abundance) is described. The quadrupole moment of these nuclei interact with the surrounding electric field gradient. This interaction causes a splitting of the nuclear energy levels and these energies depend on the orientation of the nuclei with respect to the electric field gradient. These energies are labelled by $\pm m$ and are degenerate in zero applied field. Pulsed NQR techniques was used to study the $\frac{1}{2} - \frac{3}{2}$ transition of ^{121}Sb which has a transition frequency of 11.5289 MHz. We report on our measurements of spin-lattice relaxation times in this system at low temperatures.

3.2 Korringa Relaxation

In solids, the relaxation of nuclei in metals is much more effective than in insulators. Aside from the relaxation due to the coupling to lattice vibrational modes and other motion, there is an additional relaxation process due to the presence of the conduction electrons. The discussion of this relaxation of nuclei in metals due to the nucleus-electron interaction follows that of Slichter [21]. The nucleus-conduction electron interaction can be described in terms of a scattering process. An incoming conduction electron with spin $\boldsymbol{s}$ and momentum $\boldsymbol{k}$ interacts with a nucleus and comes out with a new spin $\boldsymbol{s'}$ and momentum $\boldsymbol{k'}$. The nuclei absorb or release energy to the electrons using this basic scattering mechanism and this leads to spin-lattice relaxation of nuclei in metals. One can express the relaxation rate as

$$W_{m\boldsymbol{k}s,n\boldsymbol{k'}s'} = \frac{2\pi}{\hbar}\left|\langle m\boldsymbol{k}s|V|n\boldsymbol{k'}s'\rangle\right|^2 \delta(E_m + E_{\boldsymbol{k}s} - E_n - E_{\boldsymbol{k'}s'}) \tag{3.1}$$

where the interaction V is given by

$$V = \frac{8\pi}{3}\gamma_e\gamma_n\hbar^2\boldsymbol{I}\cdot\boldsymbol{S}\delta(\boldsymbol{r}). \tag{3.2}$$

To understand the temperature dependence, one needs to know that for the scattering process, the initial states are from within the fermi surface $f(E)$ and the final states are outside the fermi surface $1 - f(E)$. This is shown in Fig. 3.1. The relaxation rate W is then proportional to the available states given by the product $f(E)[1 - f(E)]$, which is in turn proportional to the thermal energy k_BT.
Formally,

$$W = \frac{64}{9}\pi^3\hbar^3\gamma_e^2\gamma_n^2\langle|u_k^2(0)|\rangle_{E_F}^2\rho^2(E_F)k_BT. \tag{3.3}$$

This is also related to the Knight Shift given by

$$\frac{\Delta H}{H} = \frac{8\pi}{3}\langle|u_k(0)|\rangle_{E_F}^2\chi_e^2 \tag{3.4}$$

through the electron susceptibility given by

$$\chi_o^S = \frac{\gamma_e^2\hbar^2}{2}\rho_o(E_F) \tag{3.5}$$

for a Fermi gas of non-interacting spins. We can use this non-interacting approximation to obtain the Korringa relation

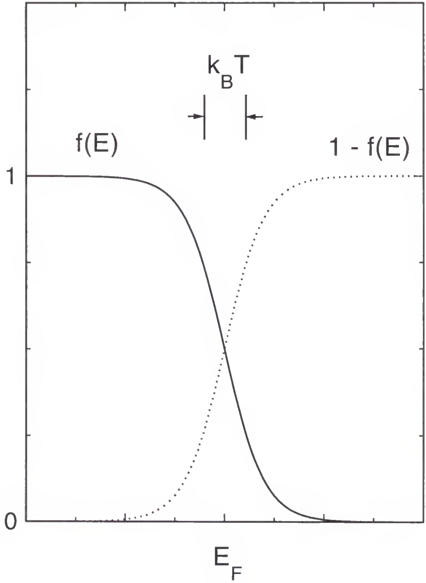

Figure 3.1: Plot of $f(E)$ and $1 - f(E)$. The overlap between these functions is proportional to kT.

$$T_1\left(\frac{\Delta H}{H}\right)^2 = \frac{\hbar}{4\pi k_B T}\left(\frac{\gamma_e^2}{\gamma_n^2}\right). \tag{3.6}$$

The product T_1T is a constant known as the Korringa constant:

$$T_1T = \frac{\hbar}{4\pi k_B}\frac{\gamma_e^2}{\gamma_n^2}\frac{1}{\left(\frac{\Delta H}{H}\right)^2}. \tag{3.7}$$

For Sb metal, T_1T was found to be constant from 77 to 4.2 K, in accordance with Korringa law [23, 24]. This shows that the dominant contribution to the spin-lattice relaxation rate comes from the interaction with the conduction electrons at the Fermi surface.

The Korringa constant given by Eq. 3.7 also provides an estimate of the electron probability density through Eq. 3.4. This estimate can be compared with the free atom probability density. Using this comparison, it is found that the s-wave carriers are the dominant contributors to the relaxation rate [23].

3.3 Other Sources of Relaxation

Aside from magnetic relaxation, relaxation is also possible via the electric interaction. Time varying electric sources can couple to the nuclear quadrupole moment and these can induce transitions between energy levels, providing a means of relaxation. The relaxation rate W_Q due to the quadrupolar interaction has two parts, W_{Q1} and W_{Q2}, corresponding to the transitions $\Delta m = 1$ and $\Delta m = 2$. These electric sources are mainly the fluctuations in the electric field gradient (EFG) at the site of the nuclei due to the motion of the ions about their equilibrium positions. One phonon and two phonon mediated relaxation is possible. In the presence of these electric relaxation, the relaxation matrix $\underline{A}$ in Eq.1.22 becomes

$$\underline{A} = \underline{A}^{(M)} + \underline{A}^{(Q1)} + \underline{A}^{(Q2)}. \tag{3.8}$$

The complete solution of the relaxation proceeds in a similar way to that outlined in Chap. 1 except that the solution contains additional exponential terms to Eq. 1.24. The electric relaxation rate W_Q is proportional to T^7 for $T \ll \theta_D$ and proportional to T^2 for $T > \theta_D$ [22]. $\theta_D = 210$ K for Sb. These relaxation mechanisms are significant only at high temperatures. At 4.2 K, the contribution of W_Q to the total relaxation rate is only 1.5% [23].

3.4 Relaxation Time Measurements

The spin-lattice relaxation time measurements of the $(\frac{3}{2} - \frac{1}{2})$ transition were made by using a pulse sequence shown in Fig. 3.2. The first pulse saturates the nuclear spins to zero magnetization. Then, after a time t, short inspection pulses are applied to measure and follow the time dependence of the magnetization $M(t)$ as it recovered from zero to its equilibrium value. The quantity $M_o - M(t)$ is proportional to the population difference $U(t)$ whose relaxation back to equilibrium is given by Eq. 1.24.

This pulse sequence was chosen over other pulse sequences because of the minimum number of pulses used. $M(t)$ can be obtained from the FID immediately following the short inspection pulse. The other alternative in measuring $M(t)$, generating spin echoes, was not used because it requires two long pulses and would generate more heating.

The width of the saturation pulse was found by monitoring the magnetization immediately after the saturation pulse. Full saturation should result in no magnetization. The saturation pulse was found to be 10.6 μs. The repetition time between each saturation pulse - delay - inspection pulse sequence was at least several times T_1, of order several hundred seconds at the lowest temperature. The T_1s used were the longest characteristic times expected, the Korringa T_1s.

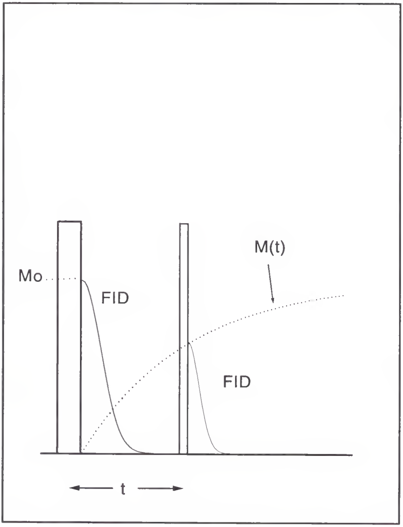

Figure 3.2: The saturation recovery pulse sequence. After saturation, the magnetization is zero. The recovery back to its equilibrium value is monitored by an inspection pulse.

At higher temperatures, more averaging was done because of the decreased signal intensity. To help reduce heating effects at the lower temperatures, shorter inspection pulses were employed and long waiting times used between the pulse sequence as dictated by the long T_1s. The FIDs following an inspection pulse (without the saturation pulse) was used to ascertain the sample temperature.

3.5 Results

Figure 3.3 shows a magnetization recovery curve taken at 6 mK. The magnetization recovery curve followed closely the double exponential of the form

$$M_\circ - M(t) = A\left\{0.107exp(-3t/T_1) + 0.893exp(-10t/T_1)\right\} \qquad (3.9)$$

expected for a spin $\frac{5}{2}$ system [4, 23], as discussed in chapter 1. $M_\circ$ is the equilibrium magnetization value. T_1 values are determined by fitting Eq. 3.9 to the magnetization recovery curve. It should be noted here that in the case of NQR, for spins $I > \frac{1}{2}$, the time constants are a fraction of T_1. T_1 measurements were made at several temperatures from 150 mK down to 1.2 mK. It was also observed that the sample cooled immediately after each demagnetization to the new temperature indicated by the size of the FID, down to about 2 mK.

We show in Fig. 3.4 the measured T_1T (the Korringa 'constant') as a function of temperature. The data at high temperatures are comparable with the measured Korringa constant of 3.5 and 4.2 s-K measured at 4.2 K obtained by other workers [23, 24] and from our previous work. These values are indicated by the dashed lines shown in the figure. However, below 75 mK we see a downturn in the T_1T product from its high temperature value of about 3.5 s-K to about 0.75 s-K at the lowest temperature. This indicates that the relaxation rate is more effective than that expected from the Korringa mechanism.

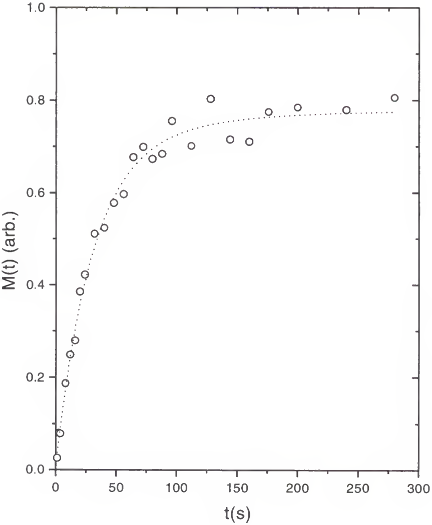

Figure 3.3: Magnetization recovery curve at 6 mK. The dashed line represents the best fit theoretical curve using Eq. 3.9.

Heating effects could lead to the observed behavior since at high temperatures, the relaxation is more effective. Heating effects can come from the RF amplitude H_1, the RF pulse width(s) t_w, and the repetition rate of the pulse sequence. The effects of all these contributions can be summarized as a heating factor defined by MacLaughlin *et al.* [4]:

$$Heating\ Factor = (Repetition\ Rate) \times H_1^2 \sum_{pulses} t_w. \tag{3.10}$$

As a check, the repetition rate and the pulse widths were varied and were found to have no effect on the measured relaxation time T_1, thus ruling out heating effects.

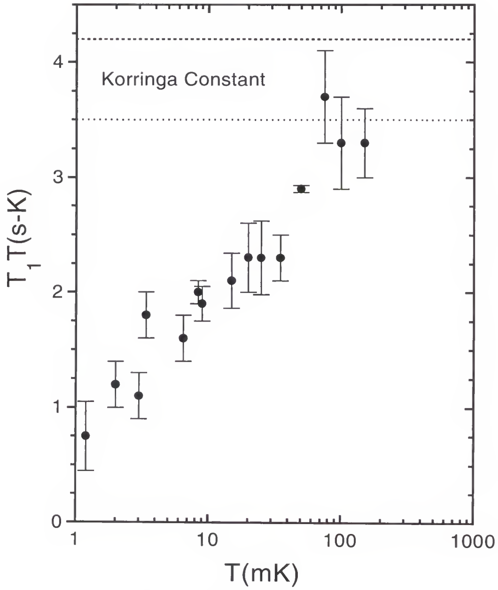

Figure 3.4: Plot of T_1T vs. Temperature. Korringa constants measured by other groups at high temperatures are indicated by the dashed lines.

CHAPTER 4
SPIN COUPLING OF Sb TO ^{3}He

4.1 Introduction

In the previous chapter, results from nuclear spin-lattice relaxation measurements of powdered metallic Sb samples immersed in liquid ^{3}He were reported in the temperature range from approximately 1.25 mK to 150 mK. The results have shown that the total nuclear spin-lattice relaxation is significantly enhanced with respect to the Korringa relaxation below 75 mK. This is attributed to the presence of a surface relaxation mechanism due to the modulation of the ^{3}He-Sb nuclear spin-spin coupling by the quantum zero-point motion of the ^{3}He atoms at the surface of the metallic particles. Similar processes have been reported for liquid ^{3}He in contact with insulators.

The Korringa relaxation process and surface relaxation mechanism have different temperature dependences. The former leads to a T_1 which is inversely proportional to temperature, while the latter is temperature independent. Because of this, the two relaxation processes can be separated by using a relaxation analysis used for studies of 2-phase media [25] or granular/porous media [26].

4.2 Bulk and Surface Relaxation Analysis

For powder, granular or porous media experiments, the surface contribution to the total relaxation can be significant. Since the surface is at the boundary of the volume of the bulk region, diffusion is also an important consideration in sorting out the bulk and surface contributions to the total relaxation. In the simplest view, consider the case where the surface relaxation centers are stronger than the bulk relaxation. After excitation of all the spins, the surface spins relax faster than the bulk spins. This creates a magnetization gradient in the direction normal to the surface. The bulk unrelaxed spins, in the presence of this gradient, will propagate to the surface by spin diffusion. In this simple physical picture, the measured relaxation time T_1^{meas} will be the total surface relaxation time plus the time it takes to travel to the surface by diffusion, that is

$$T_1^{meas} = \tau_D + \left(\frac{n_v}{n_s}\right) T_{1,s} \tag{4.1}$$

where τ_D is the diffusion time, n_v and n_s are the number of bulk and surface spins respectively, and $T_{1,s}$ is the surface relaxation time. To see the surface relaxation,

$$\tau_D < \left(\frac{n_v}{n_s}\right) T_{1,surf} \tag{4.2}$$

that is, the surface is the bottleneck in the relaxation process. This is the "fast diffusion" or "surface limited" case [27].

For insulators, spin diffusion proceeds via the dipolar interaction between nuclei. In metals, there is an additional contribution due to the indirect exchange interaction between the nuclear spins which is mediated by the electrons. This indirect exchange interaction can be one to two orders of magnitude stronger than the classical dipolar interaction in metals. Both of these interactions contribute to the diffusivity which can be written as

$$D = D_{dip} + D_{ind}. \tag{4.3}$$

The strengths of these couplings can be inferred from the spin-spin relaxation time T_2, a measure of the equilibration time between spins. The spin diffusion can be estimated from

$$D \sim \frac{a^2}{T_2} \tag{4.4}$$

where a is the inter-nuclear distance and T_2 is the spin-spin relaxation time, found to be approximately 15 μs from spin echo measurements. Using $a \sim 3$ Å, $D \sim 6 \times 10^{-11} \frac{cm^2}{s}$.

The diffusion time is given by

$$\tau_D = \frac{r^2}{6D} \tag{4.5}$$

where r is the characteristic length of the sample. For our case, r is equal to the skin depth, the length along the direction of the magnetization gradient. Because the skin depth is less than the size of the particles, there is no distribution in the characteristic length. A distribution would complicate the analysis. Using $r = 1$ μm, the skin depth in the metallic particles, $\tau_D \sim 20$ sec. As long as the total surface relaxation is longer than this diffusion time, the contribution of the diffusion time to the measured total surface relaxation will be minor.

During the unrelaxed spin's travel to the surface by spin diffusion, the bulk relaxation is effective. To take the bulk relaxation into consideration, we separate the sample into two phases: the bulk phase and the surface phase, each having its own relaxation time. If the surface phase is small ($n_s \ll n_v$) but with a faster relaxation time ($T_{1s} \ll T_{1b}$), the relaxation observed proceeds with a single relaxation rate given by [25, 28]

$$\frac{1}{T_1} = \frac{1}{T_{1,b}} + \frac{1}{T_{1,s} + \tau_s} \left(\frac{n_s}{n_v}\right) \tag{4.6}$$

where τ_s is the mean lifetime in the surface region. This lifetime can be estimated from the average time the diffusing spins spend within the thin surface region:

$$\tau_s = \left(\frac{n_s}{n_v}\right) \tau_D. \tag{4.7}$$

With $\frac{n_s}{n_v} \simeq 5 \times 10^{-4}$, $\tau_s \simeq 0.01$ sec. and thus $\tau_s \ll T_{1s}$. With these values, Eq. 4.6 can be rewritten as

$$\frac{1}{T_1} = \frac{1}{T_{1,b}} + \frac{1}{T_{1,s}} \left(\frac{n_s}{n_v}\right). \tag{4.8}$$

The observed relaxation rate is just the weighted average of the relaxation rates of the two phases.

4.3 ^{3}He-mediated Surface Relaxation

The bulk liquid ^{3}He is separated from the solid boundary by one or two layers of ^{3}He atoms. These layers, which are formed by the Van der Waals interaction between the ^{3}He atoms and the substrate atoms, are solid-like with a density similar to bulk solid ^{3}He at high pressure ($\sim$ 100 bars), the first layer being denser than the second [29]. The presence of this solid-like layer at the boundary has significant contributions to the magnetic properties of this system as shown by Ahonen *et al.* [30].

The liquid component has a magnetic susceptibility which behaves differently depending on the temperature. The liquid magnetic susceptibility is temperature independent (the Pauli paramagnetism for a Fermi liquid) for temperatures less than T_F^{**}, the magnetic Fermi temperature. For liquid ^{3}He , this temperature is about 540 mK [31]. Above this temperature, the magnetic susceptibility of the liquid ^{3}He has a Curie behavior. The solid layer component has a magnetic susceptibility which behaves according to the Curie-Weiss behavior with a positive Weiss temperature θ_W of 0.55 mK [32]. For comparison, in bulk solid ^{3}He , the magnetic susceptibility also obeys a Curie-Weiss behavior but with a negative θ_W of 1.6 mK.

The surface ^{3}He atoms are tightly bound to the surface and thus are more restricted in motion. However, they still have considerable motion even in this solid-like state. The quantum zero-point motion of the atoms leads to exchange motion and this constitutes an exchange bath or reservoir which can mediate processes with different energies of excitation. The two spin species on either side of the surface need the motion of ^{3}He atoms to take up the energy difference for cross relaxation to occur.

Magnetic cross-relaxation between ^{3}He and several types of nuclei has been studied quite extensively [33, 34] and this phenomenon has been found in several ^{3}He - substrate (insulator) systems [35]. The enhancement of the relaxation rate due to the surface ^{3}He atoms can be up several orders of magnitude compared to other mechanisms at low temperatures. It was first shown by Sullivan [36] that the the motion of the ^{3}He ad-atoms plays a key role in this surface relaxation process. The ^{3}He atoms in the solid-like first layer are very mobile due to their random quantum zero-point motion on the substrate. This motion modulates the direct dipole-dipole interaction between the ^{3}He and the substrate spins and provides a mechanism for surface relaxation.

There are two main features of this relaxation mechanism. One is that since the motion of the ^{3}He atoms is due to quantum tunneling, this relaxation mechanism is temperature independent. The other is that this mechanism is effective over a wide range of frequencies although it becomes less effective at high frequencies than at low frequencies. Experimentally, the surface relaxation rate has been found to have an ω^{-1} behavior by Schuhl *et al.* [37] and Hammel *et al.* [38]. This dependence is shown in Fig. 4.1, where data by Hammel *et al.* [38, 32] are reproduced. They studied the relaxation rate of a ^{19}F -^{3}He system and showed that the surface relaxation mechanism is effective even at high frequencies although relaxation rate decreases with frequency. In Fig. 4.1, the data cannot be fitted by a Lorentzian function (shown by the dashed line) with a single correlation time. The frequency behavior of the relaxation rate points to a distribution of correlation times.

In the discussion, it has been assumed that the surface spins consisted of the single layer of atoms at the surface. However, the effectivity of the ^{3}He layer in relaxing the substrate spins can extend to at least 2-3 layers deep into the bulk. This has been demonstrated in experiments where the substrate was pre-plated with ^{4}He or N_2 before putting in ^{3}He [39, 40]. In these experiments, the substrate spins still experienced enhanced surface-mediated relaxation although not to the same degree as when there was no buffer layer.

4.4 Relaxation analysis of Sb coupled to liquid ^{3}He

Using pulsed NQR measurements, we have observed the relaxation rate enhancement in antimony (nuclear spin $I = \frac{5}{2}$), a metallic quadrupolar system, in contact with liquid ^{3}He . By lowering the temperature, we observe the crossover in relaxation pathway from the usual nuclei-conduction electron (Korringa) relaxation mechanism to the surface ^{3}He -mediated relaxation. The random motion of the surface ^{3}He atoms [36] modulates the ^{3}He -substrate dipole-dipole interaction, and this is responsible for the enhancement of relaxation rates.

Figure 4.2 shows the measured T_1T as a function of temperature. For a metallic system, where the relaxation is due to the conduction electrons, the relaxation time follows the Korringa law:

$$T_{1,\mathrm{K}}T = \kappa \tag{4.9}$$

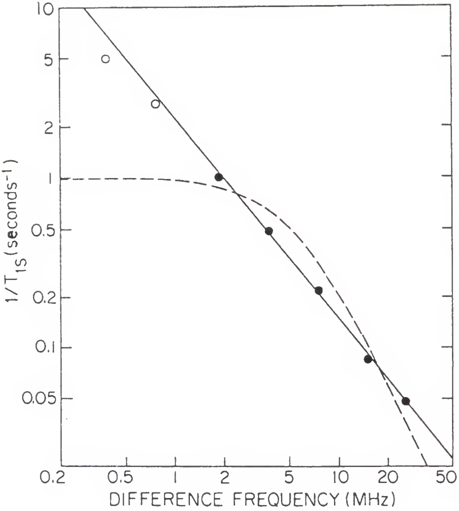

Figure 4.1: Dependence of the surface relaxation rate of ^{19}F on the difference between the Larmor frequencies of ^{19}F and ^{3}He. Reproduced from Hammel *et al.* [38]. The open circles are data from Hammel and Richardson [32].

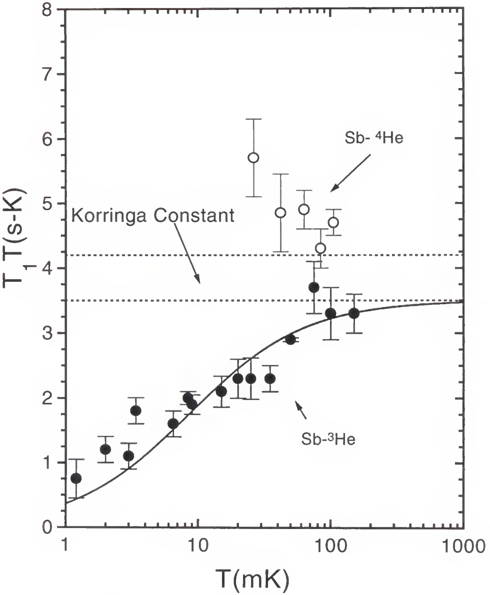

Figure 4.2: Plot of T_1T vs. Temperature. Data for the sample immersed in liquid ^{3}He and ^{4}He is shown. The solid line is the fit through the data using Eq. 4.11.

where κ is the Korringa constant and $T_{1,K}$ is the Korringa relaxation time. From previous studies, relaxation in antimony obeys the Korringa law and our high temperature data agree well with the value obtained by other workers [23, 24]. However, below 75 mK we see a downturn in the T_1T product from its high temperature value, indicating that the surface relaxation mechanism is starting to become the dominant relaxation pathway. Application of a small magnetic field (about 15 gauss) at 15 mK did not significantly change the T_1.

Combining Korringa's law for the bulk spins with the temperature independent relaxation rate for surface relaxation, we arrive at the following expression for T_1 following Eq. 4.8:

$$\frac{1}{T_1} = \frac{1}{T_{1,\mathrm{K}}} + \frac{1}{T_{1,s}} \left(\frac{n_s}{n_v}\right) \tag{4.10}$$

where we have replaced $T_{1,av}$ with T_1. Using Eq. 4.9, the Korringa law, and rearranging to get an expression for T_1T, we get

$$T_1T = \frac{\kappa T_{1,s}^{tot} T}{(\kappa + T_{1,s}^{tot} T)} \tag{4.11}$$

where $T_{1,s}^{tot} = T_{1,s}\frac{n_v}{n_s}$ is the temperature independent surface relaxation time due to the presence of ^{3}He on the surface. Using the experimentally determined value for the Korringa constant, $\kappa = 3.5$ s-K [23, 24], we can find a good fit to our data using Eq. 4.11, with $T_{1,s}^{tot}$ =410 sec.

We can also estimate the relaxation time of the surface Sb spins, $T_{1,s}$, by multiplying $T_{1,s}^{tot}$ with n_s/n_v, the ratio of the number of surface atoms to the number of atoms within the bulk (i.e. within the skin depth of 1μm). We estimated n_s/n_v to be around 5×10^{-4}, from which we obtain $T_{1,s} \approx 0.2$ sec.

Finally, the origin of the relaxation process that is more effective than the Korringa process at low temperatures is confirmed by replacing the liquid ^{3}He with liquid ^{4}He. The relaxation times were measured again and the results are shown in Fig. 4.2. The relaxation times become longer, corresponding to their bulk value, than when the powdered sample is in contact with liquid ^{3}He .

4.5 Sb-^{3}He coupling model

In this section, the coupling between the internal components of Sb and ^{3}He is briefly discussed. These components are distinct and each has a definite temperature i.e. within these components, the internal equilibration is very fast. For the Sb, the components are the bulk nuclei, the electrons, the phonons, and the surface nuclei. For ^{3}He, we have the surface and the bulk liquid components. These components are shown in Fig. 4.3.

For Sb, the coupling between the electrons and the nuclei (in the bulk as well as the surface) is characterized by the Korringa time T_1. Equilibration among neighboring nuclear spins is of order T_2. In the presence of a magnetization gradient, the transit time of the bulk magnetization to the surface is τ_D, the diffusion time, which depends on the distance to the surface.

Across the interface, it has been shown that the coupling between the substrate surface spins and the ^{3}He atoms on the surface is quite strong, being under 1 sec. Because of the large amount of the liquid ^{3}He, it can be considered to be at the thermal bath. Among the components, the Sb electrons have the lowest heat capacity.

4.6 Conclusion

For powdered metallic particles (with $I \neq 0$) immersed in liquid ^{3}He, it has been found that a surface relaxation process, previously found and studied in insulating

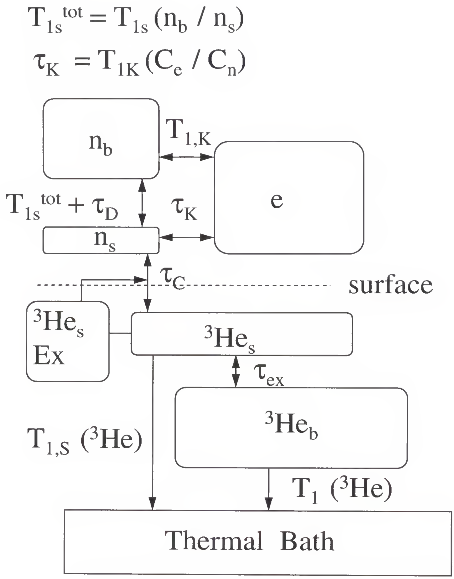

Figure 4.3: Block diagram showing the couplings between the components of the Sb and ^{3}He .

systems, becomes more effective than the Korringa relaxation as the temperature is lowered. This surface relaxation process is due to the modulation of the dipole-dipole interaction between the ^{3}He atoms on the surface and the surface spins. This effect is very general and can be considered to be characteristic of powdered metals (whose nuclei have magnetic moments) in liquid ^{3}He .

Among the parameters to be considered which affect the effectiveness of this relaxation process are the characteristic length (grain size or skin depth) of the metal particle, the Korringa constant, and the frequency. The characteristic length determines the diffusion time to the surface. A faster diffusion time means that the surface relaxation dominates the total relaxation. The smaller the particle or the shorter the skin depth, the more observable the surface effects. The Korringa constant κ determines the coupling between the electrons and the nuclei. The magnitude of the κ determines the "cross-over temperature" from the Korringa dominated high temperature region to the low temperature region where the surface relaxation becomes more dominant than the Korringa relaxation. This "cross-over" temperature is the temperature at which a deviation from the Korringa law starts to occur. This cross-over temperature is lower for metals with smaller Korringa constants like Cu, Pt with Korringa constants of 1.24 and 0.034 s-K, respectively.

Another signature of this phenomenon is the frequency dependence. The relaxation due to the coupling between the surface ^{3}He atoms and the substrate nuclei is stronger at low frequencies and the surface relaxation becomes more effective at low frequencies. Thus the surface contribution becomes more pronounced and the "cross-over temperature" is higher at low frequencies.

There are some experimental reports on relaxation studies on platinum ($I = \frac{1}{2}$) powders immersed in liquid ^{3}He which exhibit these effects [41, 42, 43] and the data are reproduced in Fig. 4.4. In these reports, a deviation from the Korringa behavior is seen towards faster T_1's at low temperatures, with the effect being stronger at low

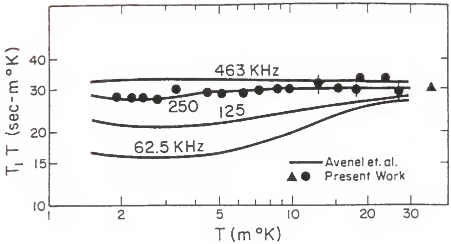

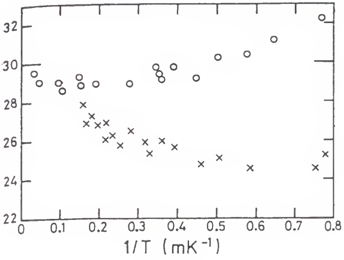

Figure 4.4: T_1T plots for powdered platinum immersed in ^{3}He. Top figure: Data from Edwards *et al.* [42] and Avenel *et al.* [43]. Bottom figure: Data from Ling *et al.* [41]. The y-axis has units of sec-mK. The open circles are data using a frequency of 125 kHz and the crosses are data using 62.5 kHz.

frequencies. At a frequency of 62.5 kHz the surface relaxation causes a deviation from Korringa law starting at abojt 10-20 mK. While impurities may contribute to the deviation as presumed in these reports, the effects discussed in this chapter seem to be the more likely explanation. These effects should be an important consideration in using powdered Pt immersed in liquid ^{3}He for NMR thermometry.

CHAPTER 5
POPULATION DIFFERENCE THERMOMETRY

5.1 Introduction

In response to the need for primary thermometers at ultra-low temperatures, several schemes based on population difference thermometry [44] have been suggested using NMR/NQR techniques [45, 46, 47]. In thermal equilibrium, the population of each energy level of a particular nuclear-spin system obeys a temperature dependence given by the Boltzmann distribution. At low temperatures, the lower levels become more populated relative to the higher energy levels. As a consequence, the relative intensities of the transitions between adjacent levels become more asymmetric at low temperatures when the energy separation becomes comparable to the temperature. Nuclear resonance techniques can measure the intensities of these transitions and provide an indication of the population difference between the levels. Factors introduced by the measuring system can be removed by taking the ratio of two transitions. The intensity ratio of two absorption lines, which is used as a measure of the asymmetry, follows a function which depends only on the energies and the temperature and this can be used for thermometry.

5.2 Principles

For a spin system in thermal equilibrium, with energy levels E_i, the thermal population P_i of each level obeys the Boltzmann distribution and is given by

$$P_i = Nexp(\frac{-E_i}{k_B T}) \tag{5.1}$$

where N is the total number of spins, k_B is Boltzmann's constant and T is the temperature. An example of such a system is a collection of nuclei with spin I in a magnetic field. The magnetic field splits the energy into several levels according to the orientation of the dipole moment with respect to the magnetic field, each characterized by the quantum number m ($-I < m < I$). Another example is a quadrupolar system which interacts with an electric field gradient. The energy levels correspond to different orientations of the quadrupole moment relative to the electric field gradient. Each level is characterized by m^2. The frequencies of the tranistions between these levels are in the radiofrequency range and can be probed by nuclear resonance methods.

The intensity I_i of each transition between the levels i and $i+1$, with frequency $\omega_i = (E_{i+1} - E_i)/\hbar$, is proportional to the population difference $P_i - P_{i+1}$. Taking the ratio removes the proportionality factor relating the intensity to the population difference. The ratio of the intensities of two such transitions I_i and I_j is

$$\frac{I_i}{I_j} = \frac{P_i - P_{i+1}}{P_j - P_{j+1}}. \tag{5.2}$$

In terms of the frequencies,

$$\frac{I_i}{I_j} = exp(-\frac{\hbar\Delta\omega}{k_B T})\left\{\frac{1 - exp(-\frac{\hbar\omega_i}{k_B T})}{1 - exp(-\frac{\hbar\omega_j}{k_B T})}\right\} \tag{5.3}$$

where $\hbar\Delta\omega = E_i - E_j$. The intensity ratio depends only on the energies and the temperature. Measuring the intensity ratio therefore allows a determination of the absolute temperature while removing other factors introduced by the measuring system.

5.3 Magnetic Field Perturbed NQR

5.3.1 Angular Dependence of the Frequencies

In this section, a quadrupolar system perturbed by a small magnetic field is studied for the purpose of implementing thermometry based on population differences. As discussed in the first chapter, for a nuclear spin $I > \frac{1}{2}$ with quadrupole moment Q in an axially symmetric electric field gradient q, the energies are degenerate in m in zero field and are given by

$$E_{\pm m} = A[3m^2 - I(I+1)];\ A = \frac{e^2qQ}{4I(2I-1)}. \tag{5.4}$$

There are $I+\frac{1}{2}$ doubly degenerate levels for half integral spins and I doubly degenerate (except $m = 0$) levels for integral spins. Transitions between levels m and $m+1$ can be induced by RF fields at the angular frequency of transition $\omega_m = (E_{m+1} - E_m)/\hbar$. Using Eq. 5.4, the angular frequencies of transition are

$$\omega_m = \frac{3A}{\hbar}(2|m|+1). \tag{5.5}$$

A small magnetic field H_o ($\gamma H_o << e^2qQ$) lifts the degeneracy in m and the new energies are [2], for $|m| > \frac{1}{2}$,

$$E_{\pm m} = A[3m^2 - I(I+1)] \mp m\hbar\gamma H_o cos\theta \tag{5.6}$$

and for $|m| = \frac{1}{2}$,

$$E_{\pm} = A[\frac{3}{4} - I(I+1)] \mp \frac{f}{2}\hbar\gamma H_o cos\theta \tag{5.7}$$

where $f = \sqrt{1 + (I + \frac{1}{2})^2 tan^2\theta}$ and θ is the angle between the external field H_o and the symmetry axis of the electric field gradient q. The $m = \pm\frac{1}{2}$ case is treated differently because of mixing between the states [2]. These states are

$$\begin{aligned} |+\rangle &= sin\,\alpha\,|\frac{1}{2}\rangle + cos\,\alpha\,|-\frac{1}{2}\rangle & (5.8) \\ |-\rangle &= -cos\,\alpha\,|\frac{1}{2}\rangle + sin\,\alpha\,|-\frac{1}{2}\rangle & (5.9) \end{aligned}$$

where $tan\,\alpha = \sqrt{\frac{f+1}{f-1}}$.

For this work, the $(\frac{3}{2} - \frac{1}{2})$ transition of ^{121}Sb with an RF transition frequency $\nu_{\frac{1}{2}}$ of 11.5289 MHz and its splitting are studied for a small perturbing magnetic field. The allowed transitions ($\Delta m = 1$)between the $\pm\frac{3}{2}$ and the $\pm\frac{1}{2}$ levels of the mixed states $|+\rangle$ and $|-\rangle$ are illustrated in Fig. 5.1. The transition $|-\rangle$ to $|+\rangle$, while allowed, is low frequency and below the range of detection.

In Fig. 5.2, the full angular dependence of the energy levels given by Eqs. 5.6 and 5.7 are shown.

The frequencies of these transitions are given by

$$\omega_{a\pm} = \omega_{\frac{1}{2}} \pm \frac{(3-f)}{2}\gamma\hbar H_o cos\theta \qquad (5.10)$$

$$\omega_{b\pm} = \omega_{\frac{1}{2}} \pm \frac{(3+f)}{2}\gamma\hbar H_o cos\theta. \qquad (5.11)$$

Figure 5.3 shows the plot of the frequencies $\omega_{a\pm}$ and $\omega_{b\pm}$ as a function of the angle θ. In the figure, ω_{a+} is denoted as ω_{a1}, etc.

The splitting is symmetric about $\omega_{\frac{1}{2}}$ and consists of two pairs a and b. The a pair is the inner pair for θ between 0° and 90° and becomes the outer pair for θ between 90° and 180°. Likewise, the b pair is the outer pair for θ between 0° and 90° and becomes

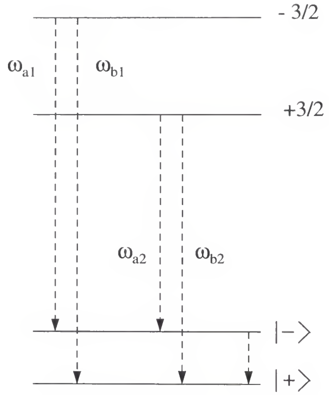

Figure 5.1: Schematic representation of the allowed transitions between the $\pm\frac{3}{2}$ and the $\pm\frac{1}{2}$ states of the mixed states $|+\rangle$ and $|-\rangle$ (See text).

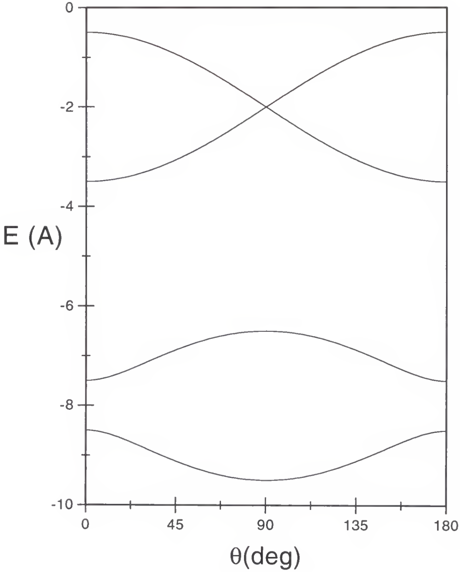

Figure 5.2: Angular dependence of the energy levels of the $|\pm\frac{3}{2}\rangle$ (top) and the $|\pm\rangle$ (bottom) states.

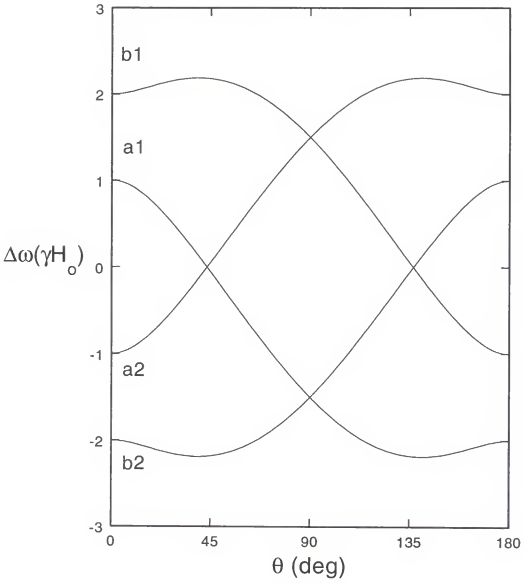

Figure 5.3: Angular dependence of the frequency splitting of the $\frac{3}{2}-\frac{1}{2}$ transition for a spin $I=\frac{5}{2}$ nucleus in a weak magnetic field.

the inner pair for θ between 90° and 180°. In addition to the angular dependence of the frequencies, there is also an angular dependence of the intensity of each pair. The intensity of the a pair is $I_a = \frac{(f+1)}{f}$ and for the b pair, $I_b = \frac{(f-1)}{f}$. With this angular dependence, the a pair is maximum at 0°, where it is the inner pair, and decreases monotonically to zero at 180° where it is the outer pair. Likewise, the intensity of the b pair is zero at 0°, where it is the outer pair, increases and becomes maximum at 180° where it is the inner pair. In addition to these angular dependences, there is an additional $sin^2\theta$ dependence for both pairs due to the fact that the RF excitation is effective only at a direction perpendicular to the RF coil which is in the same direction as the external magnetic field H_o. This has been discussed in the first chapter. The angular dependence of the intensity is shown in Fig. 5.4.

5.3.2 Powder Pattern

For a powder sample, the crystallites are randomly oriented and therefore all orientations are equally likely. The number of crystallites oriented at an angle between θ and $\theta + d\theta$ is proportional to $sin\theta\, d\theta$ ($= d\mu$ with $\mu = -cos\theta$). Since the frequency ω depends on θ, there will be a distribution of ω's reflecting the distribution of orientations.

The intensity is proportional to the number of crystallites and therefore the intensity $g(\omega)d\omega$ with frequencies between ω and $\omega + d\omega$ is proportional to the number of crystallites $d\mu = |d\mu/d\omega|d\omega$. The lineshape $g(\omega)$ is then given by

$$g(\omega) \sim \left|\frac{d\mu}{d\omega}\right|. \tag{5.12}$$

Since ω is given as a function of angle (or μ), the prescription for obtaining $g(\omega)$ is to invert $\omega(\mu)$ to get $\mu(\omega)$ and then get the derivative $d\mu/d\omega$.

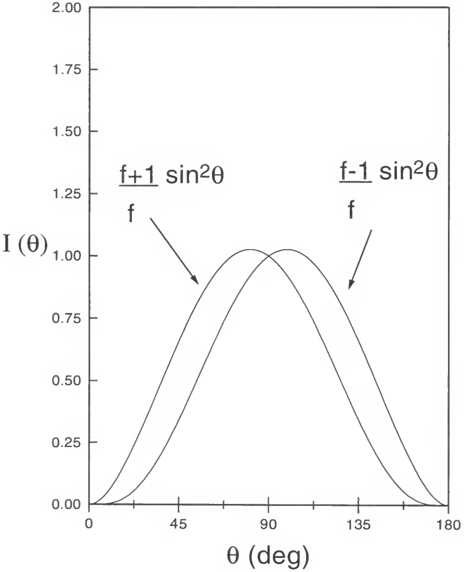

Figure 5.4: Angular dependence of the intensity of the *a* branch and the *b* branch. See text for discussion.

Consider first the branch ω_{a1} with frequency given by Eq. 5.10. Using $\omega = \omega_{a1} - \omega_{\frac{1}{2}}$ and $\mu = -cos\theta$,

$$\omega = -3\mu - \sqrt{9 - 8\mu^2} \tag{5.13}$$

where ω is in units of $\frac{1}{2}\gamma\hbar H_o$. Solving for μ,

$$\mu = \begin{cases} \frac{-3\omega - \sqrt{153 - 8\omega^2}}{17} & \begin{matrix} -1 < \mu < 0.7717 \\ \text{and } -4.373 < \omega < 2 \end{matrix} \\ \frac{-3\omega + \sqrt{153 - 8\omega^2}}{17} & \begin{matrix} 0.7717 < \mu < 1 \\ \text{and } -4.373 < \omega < -4 \end{matrix} \end{cases} . \tag{5.14}$$

Taking the derivative,

$$\frac{d\mu}{d\omega} = \begin{cases} -\frac{3}{17} + \frac{8\omega}{17\sqrt{153 - 8\omega^2}} & \begin{matrix} -1 < \mu < 0.7717 \\ \text{and } -4.373 < \omega < 2 \end{matrix} \\ -\frac{3}{17} - \frac{8\omega}{17\sqrt{153 - 8\omega^2}} & \begin{matrix} 0.7717 < \mu < 1 \\ \text{and } -4.373 < \omega < -4 \end{matrix} \end{cases} . \tag{5.15}$$

Using Eqs. 5.12 and 5.15, the powder pattern for this branch is then

$$g^{a1}(\omega) = g_1^{a1}(\omega) + g_2^{a1}(\omega) \tag{5.16}$$

where

$$g_1^{a1}(\omega) = \begin{cases} \left| -\frac{3}{17} + \frac{8\omega}{17\sqrt{153 - 8\omega^2}} \right| & -4.373 < \omega < 2 \\ 0 & \text{otherwise} \end{cases} \tag{5.17}$$

$$g_2^{a1}(\omega) = \begin{cases} \left| -\frac{3}{17} - \frac{8\omega}{17\sqrt{153 - 8\omega^2}} \right| & -4.373 < \omega < -4 \\ 0 & \text{otherwise.} \end{cases} \tag{5.18}$$

The other branches of the powder lineshape can be generated by symmetry using the substitutions $\omega \rightarrow -\omega$ and $\mu \rightarrow -\mu$. The complete lineshape from the angular dependence of the frequencies is

$$g(\omega) = g^1(\omega) + g^2(\omega) \tag{5.19}$$

where $g^1(\omega) = g^{a1}(\omega) + g^{b1}(\omega)$ and $g^2(\omega) = g^{a2}(\omega) + g^{b2}(\omega)$

The angular dependence of the intensity also needs to be taken into account. As discussed in the previous section, the intensity of the a pair is $I_a = \frac{(f+1)}{f} sin^2\theta$ while for the b pair, $I_b = \frac{(f-1)}{f} sin^2\theta$. Written in terms of the frequency, the intensity modulating the $g_1^{a1}(\omega)$ branch is

$$i_1^{a1}(\omega) = \left\{ \frac{-5\omega + 4\sqrt{153 - 8\omega^2}}{-8\omega + 3\sqrt{153 - 8\omega^2}} \right\} \left\{ 1 - \frac{153 + \omega^2 + 6\omega\sqrt{153 - 8\omega^2}}{289} \right\}. \tag{5.20}$$

Similarly, for the $g_2^{a1}(\omega)$, the modulating intensity function is

$$i_2^{a2}(\omega) = \left\{ \frac{-5\omega - 4\sqrt{153 - 8\omega^2}}{-8\omega - 3\sqrt{153 - 8\omega^2}} \right\} \left\{ 1 - \frac{153 + \omega^2 - 6\omega\sqrt{153 - 8\omega^2}}{289} \right\}. \tag{5.21}$$

Instead of Eq. 5.16, the complete lineshape is obtained by multiplying each branch with its corresponding intensity function. The powder pattern for the $a1$ branch becomes

$$G^{a1}(\omega) = g_1^{a1}(\omega) i_1^{a1}(\omega) + g_2^{a1}(\omega) i_2^{a1}(\omega). \tag{5.22}$$

Again, the modulating intensity functions for the other branches can be calculated by symmetry. The complete powder lineshape is then given by

$$G(\omega) = G^{a1}(\omega) + G^{b1}(\omega) + G^{a2}(\omega) + G^{b2}(\omega). \tag{5.23}$$

The calculated powder pattern $G(\omega)$ is shown in Fig. 5.5. A broadening function convoluted with $G(\omega)$ will generate the effect of experimental broadening.

There are two distinct and well resolved peaks with an angular frequency separation equal to $4.373\gamma H_o$. These frequency peaks are labelled ω_+ and ω_-. These

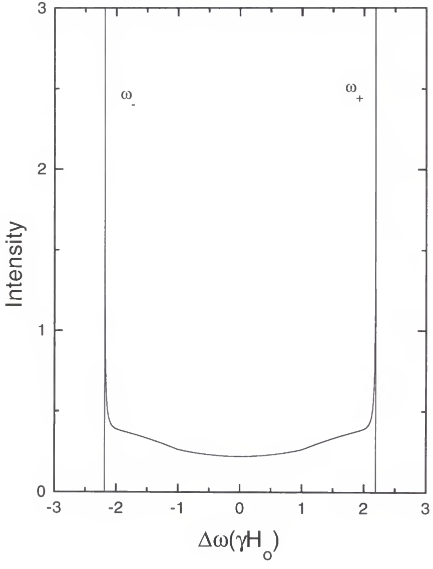

Figure 5.5: Plot of the resulting powder pattern $G(\Delta\omega)$.

intensities of these NQR lines are studied for the purpose of thermometry. For this case, Eq. 5.3 becomes

$$\frac{I_-}{I_+} = exp(-\frac{\hbar\Delta\omega}{k_BT})\left\{\frac{1 - exp(-\frac{\hbar\omega_-}{k_BT})}{1 - exp(-\frac{\hbar\omega_+}{k_BT})}\right\}. \tag{5.24}$$

5.4 Experimental Apparatus

The system studied is ^{121}Sb with nuclear spin $I = \frac{5}{2}$ (57% abundance). The same annealed high purity (99.9999%) antimony fine powder used for relaxation studies described in the previous chapters was used. About 16 mg of antimony was used. Using small amounts of the sample is necessary for efficient cooling and short thermal equilibration times.

A ^{195}Pt NMR thermometer calibrated against a ^{3}He melting curve thermometer was used to determine the temperature of the liquid ^{3}He bath. The ultrasound attenuation studies also provided an independent (though qualitative) probe of the liquid ^{3}He temperature.

A superconducting magnet, described previously in the experimental section, surrounded the assembly to provide the external magnetic field. In this arrangement, the RF coil is in the same orientation as the external field. The pulsed NQR spectrometer operated at 11.5289 MHz and had sufficient bandwidth to observe nearby frequencies. At this frequency and at low temperatures, the skin depth was estimated to be approximately 1 μm for antimony.

The two magnetic field perturbed NQR lines indicated in Fig. 5.5 were examined separately by applying a short RF pulse ($\approx 8^\circ$ tipping angle) at the resonant frequency of each line. These tipping pulses reduces the nuclear magnetization from M_n to $M_n cos\,\theta$ where θ is the tipping angle and the nuclear temperature increases from T_n to $T_n/cos\,\theta$ [48]. For the short pulses used, the increase in nuclear temperature is about 1%. Since the signal is proportional to $sin\,\theta$, a compromise needs to be made between signal size and heating effects. However, at low temperatures where heating effects are a concern, the signal also is larger. Typically, a compromise value of 10° pulses are used at low temperatures. In addition, short pulses are necessary at low temperatures to obtain the correct absorption spectrum from the Fourier transform [49].

The absorption spectra was obtained from the FIDs instead of from the spin echo for two reasons: the short RF pulse used to generate the FID probes the state of the nuclear spins just before the pulse is applied, and less heating is introduced because generating a spin echo requires two pulses.

The inspection pulses were 15-20 minutes apart, sufficient time for the system to return to equilibrium. Four FIDs following the short pulses were accumulated and took about an hour. The averaged FIDs after these short RF pulses were Fourier transformed to recover the absorption spectra. The two NQR lines magnetic field NQR lines were examined in this way and the two line spectrum was obtained in two hours. To significantly reduce heating due to leakage of the RF into the cryostat, the output of the RF signal generator was on only during the RF pulse. This greatly increases the isolation in addition to the isolation provided by the crossed diodes.

5.5 Results

The presence of the liquid ^{3}He provided a surface-mediated relaxation process which is more effective than the conduction-electron mediated relaxation (Korringa relaxation) at these low temperatures [50, 51]. This relaxation process is due to the presence of a solid-like layer of ^{3}He on the surface of the antimony particles. The quantum zero point motion of the ^{3}He atoms in this solid-like layer modulates the dipole-dipole interaction between the ^{3}He and the surface antimony nuclei. In a preliminary report [51] and as discussed in the previous chapter, from measurements of the total relaxation times, we have found that the surface relaxation time is of order 1 second. Thus for time scales greater than 1 second, the surface spins are always in equilibrium with the liquid ^{3}He .

Figure 5.6 shows the two magnetic field perturbed NQR lines labeled according to the transitions indicated in Fig. 5.5 for $H_o = 540$ gauss. The value for H_o was obtained from a calibration at very weak fields. In the figure, the spectra are shown as a composite spectra of the two lines. The two lines are clearly well separated with an angular frequency of separation $\Delta\omega$ equal to $4.373\gamma H_o$, as expected from the weak field perturbed quadrupolar powder pattern.

The difference in intensity ratio can be seen clearly between the high temperature (1.4 mK) and the low temperature (0.25 mK) spectra. Relative to that of the low frequency line, the intensity of the high frequency line increases at low temperatures.

Figure 5.7 shows the integrated intensity ratio as a function of temperature, as measured by the ^{195}Pt NMR thermometer, down to 0.25 mK.

5.6 Discussion and Conclusion

Ideally, measurement of the intensity ratio offers the possibility of absolute thermometry without the need for calibration. Shown in Fig. 5.7 is the intensity ratio predicted by Eq. 5.24 (dotted line). However, it is seen that the high temperature value of the measured intensity ratio is higher than expected value of ω_-/ω_+. The measured intensity ratio suggests a higher than expected intensity for the low frequency absorption line (or lower intensity for the high frequency line). This fact was also observed by Pollack *et al.* [47] in their work on Scandium metal.

One explanation for this behavior can simply be due to the frequency dependence of the anomalous skin depth, δ, into the metal which varies as $\omega^{-\frac{1}{3}}$. At lower frequencies, the RF field penetrates more into the metal and samples more spins and

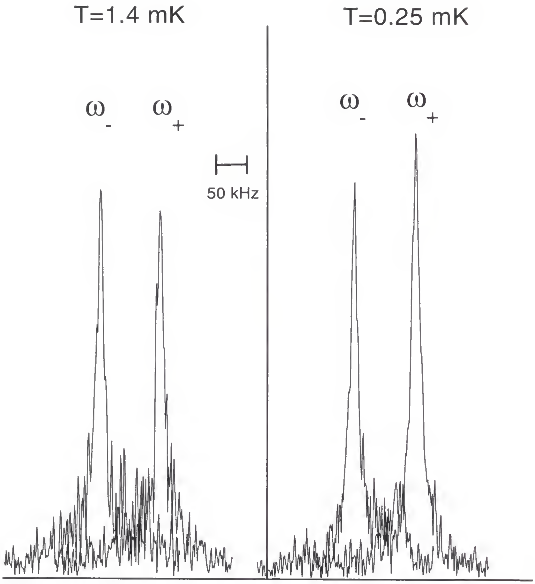

Figure 5.6: High temperature and low temperature composite spectra. The vertical scale is different for the T = 1.4 mK and the T = 0.25 mK cases.

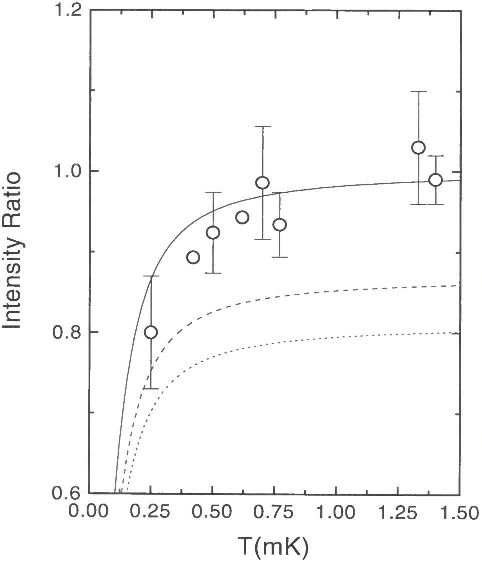

Figure 5.7: Intensity Ratio vs. Temperature. The dotted line is the theoretical intensity ratio given by Eq. 5.24, the dashed line is the intensity ratio multiplied by the skin depth correction factor, and the solid line is the intensity ratio normalized at high temperature.

thus the intensity is higher than that of the high frequency line. The intensity ratio multiplied by a skin depth correction factor is shown in Fig. 5.7 (dashed line).

Another factor can be the frequency dependent response of the detection system. NMR/NQR spectrometers are operated in the resonant mode to achieve efficient coupling during the excitation and high sensitivity detection of the FID. Unfortunately, it also makes the response frequency dependent.

Self-calibration can be performed by normalizing to the high temperature data point by multiplying the theoretical curve predicted by Eq. 5.24 with an overall factor. This self-calibrated curve is shown as the solid line in Fig. 5.7. At the lowest temperature, 0.25 mK, the temperature uncertainty is about 0.1 mK. As can be seen from the data, the high temperature data point needs to be determined more precisely as it is the internal calibration point.

Better precision can be achieved by improvements in each step of the signal detection and recovery process. First, more sample can be used, resulting in increased signal. This can be done by increasing the volume available to the sample and also by putting in some degree of packing (gently, so as not to introduce strains into the sample) instead of being loosely packed. This step has to be done without compromising cooling considerations. Secondly, on the detection side, higher sensitivities can be achieved by addressing the impedance matching considerations of the RF coil to the lossy coaxial cables. Low temperature coaxial cables are inherently lossy because low thermal conductivity materials are used. Putting the tuning capacitor at the low temperature end of the coaxial cable, instead of at the top of the cryostat, and careful consideration of impedance matching at both ends of the coaxial cable can also significantly increase the sensitivity [52].

In this study, this was not implemented because the setup with the sample RF coil alone, without cold tuning and matching capacitors, is simpler to implement and easier to handle, and was deemed the wiser (and more cautious) choice. Adding tuning elements in the cryostat can have potential problems which are harder to deal with once the cryostat is cold especially in a large cryostat when cool-down and warm-up times are long.

We have demonstrated the use of Zeeman perturbed NQR in antimony as an absolute, self calibrating population difference thermometer at ultra low temperatures. In this class of thermometers, measurement of the intensity ratio and a determination of the frequencies of two lines is needed for themometry. For the particular case of Zeeman perturbed NQR, a small external field H_o allows for flexibility in choosing the temperature range for which the thermometer is sensitive, limited only by the frequency response of the spectrometer. This feature is not possible for the other realizations of NMR/NQR based thermometry where the resonant lines are fixed. It is also interesting to note that no anomalies were observed in the NQR signals or the thermal relaxation rates down to 0.25 mK in fields as low as 0.1 gauss indicating that Sb remains a normal metal down to these values of H and T.

APPENDIX A
QUENCH CONTROL CIRCUIT

This appendix describes the operation of the quench control circuit. The quench control circuit generates two opposite polarity pulses in response to an input pulse. The output pulses have a fast rise time and a selectable fall time. This fall time is used to hasten the ringdown of the transmitter pulse, delay the switchover to the reception mode, as well as provide a smooth decay of the control pulse to prevent parasitic ringings associated with sharp fall times.

The quench control circuit diagram is shown in Fig. A.1. The inputs go through diodes D1 and D2 to the RC network. The diodes allow the generation of a pulse with a fast risetime and a smoothly decaying tail. Time constants of 2, 5, 10, and 15 μS are available by a selection of capacitors C. After the general shape of the pulse is formed, it goes to a 'long tailed pair' (Q1) which generates two pulses with opposite polarities. This goes to a high pass filter to establish 0V as the baseline. The pulses go to a follower formed by Q2 and Q3. Transistors Q4 and Q5 act as buffers. The variable resistor labeled 'balance' provides for matching the amplitudes of the two output pulses.

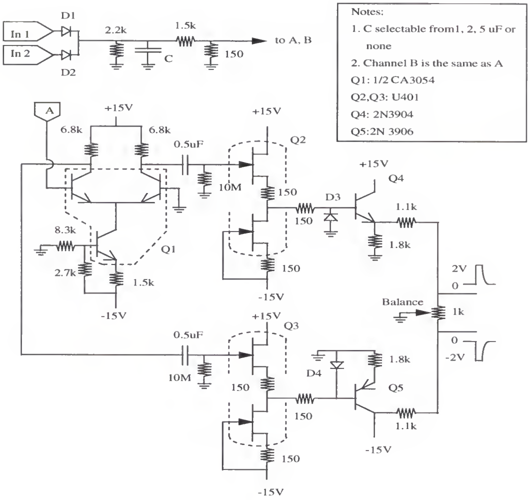
Notes:
1. C selectable from1, 2, 5 uF or none
2. Channel B is the same as A
Q1: 1/2 CA3054
Q2,Q3: U401
Q4: 2N3904
Q5:2N 3906

Figure A.1: Quench Control Circuit for the Duplexer and Tuned Limiter.

APPENDIX B
FAST AMPLIFIER

The fast amplifier used to amplify the in-phase and quadrature detected FID uses a precision instrumentation amplifier, AD 524. Among the features of this amplifier are: low noise, pin programmable gain (no external components are required to set the gain), high speed with a slew rate of $5V/\mu S$. The complete circuit is shown in figure B.1. The inputs see 50 ohms for matching and the gain is set to 10 using the appropriate pins connections.

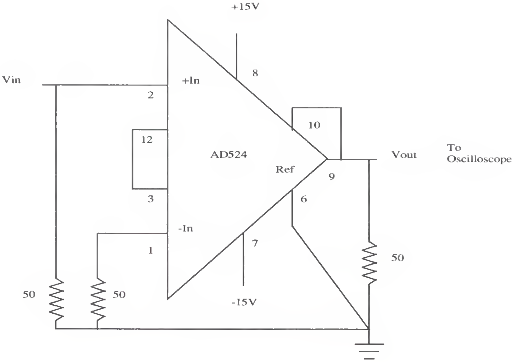

Figure B.1: Fast Amplifier Circuit Diagram Based on the AD 524 Precision Instrumentation Amplifier.

REFERENCES

[1] M.H. Cohen and F. Reif, in **Solid State Physics** vol. 5, F. Seitz and D. Turnbull, eds. (Academic Press, London 1957).

[2] T.P. Das and E.L. Hahn, *Adv. in Sol. State Phys. Suppl 1*, F.Seitz and D. Turnbull, eds. (Academic Press, London,1958).

[3] H. Enge, **Introduction to Nuclear Physics** (Addison-Wesley, 1970).

[4] D.E. MacLaughlin, J.D. Williamson, and J. Butterworth, *Phys. Rev. B* **4**, 60 (1971).

[5] M. Bloom, E.L. Hahn, and B. Herzog, *Phys. Rev.* **97**, 1699 (1955).

[6] T.P. Das and A.K. Saha, *Phys. Rev.* **98**, 516 (1955).

[7] Johnson Matthey Catalog Company Inc., Ward Hill, MA 01835.

[8] R.R. Hewitt and B.F. Williams, *Phys. Rev.* **129**, 1188 (1963).

[9] E.I. du Pont du Nemours & Co., Wilmington, DE 19808.

[10] Emerson & Cumming Inc., Canton, MA 02021.

[11] Millipore Filter Corp., Bedford,MA.

[12] G.E. Granroth, E.B. Genio, J.B. Walden, J.W. Xu, G.G. Ihas, and M.W. Meisel, *Czech. J. Phys.* **46**, 91 (1996).

[13] Apiezon Products, Ltd., 4 York Rd., London, UK.

[14] G.J. Labbe, H. Royce, Y. Takano, and G.G. Ihas, in **Quantum Fluids and Solids**, G.G. Ihas and Y. Takano, eds. (AIP, New York 1989).

[15] J. Xu, O. Avenel, J.S. Xia, M-F Xu, T. Lang. P.L. Moyland, W. Ni, E.D. Adams, G.G. Ihas, M.W. Meisel, N.S. Sullivan, and Y. Takano, *J. Low Temp. Phys.* **89**, 719 (1992).

[16] T. Lang, Ph.D. Thesis, University of Florida, 1996 (unpublished).

[17] Oxford Instruments Ltd., Oxford, U.K.

[18] G.S. Straty and E.D. Adams, *Rev. Sci. Instrum.* **40**, 1393 (1969).

[19] E.D. Adams, *Rev. Sci. Instrum.* **64**, 601 (1993).

[20] Paroscientific Inc., Redmond, WA 98052

[21] C.P. Slichter, **Principles of Magnetic Resonance 3rd ed.** (Springer-Verlag, 1990).

[22] A. Abragam, **Principles of Nuclear Magnetism** (Oxford University Press, 1989).

[23] R.R. Hewitt and D.E. MacLaughlin, *J. Mag. Res* **30**, 483 (1978).

[24] J.M. Keartland, G.C.K. Folscher, and M.J.R. Hoch, *Phys. Rev. B* **43**, 8362 (1991).

[25] H. Pfeifer, in **NMR: Basic Principles and Progress** Vol. 7, P. Diehl *et al.*, eds. (Springer-Verlag, New York, 1972).

[26] W.P. Halperin, F. D'Orazio, S. Bhattacharja, and J.C. Tarczon, in **Molecular Dynamics in Restricted Geometries**, J. Klafter and J.M. Drake, eds. (Wiley, New York, 1989).

[27] K.R. Brownstein and C.E. Tarr, *Phys. Rev. A* **19**, 2446 (1979).

[28] J. Korringa, D.O. Seevers, and H.C. Torrey, *Phys. Rev.* **127**, 1143 (1962).

[29] R.A. Guyer, in *Physics at Ultralow Temperatures*, Proceedings of the 1977 Hakone International Symposium, T. Sugawara *et al.*, eds. (Physical Society of Japan, Tokyo, 1978).

[30] A.I. Ahonen, T. Kodama, M. Krusius, M.A. Paalanen, R.C. Richardson, W. Schoepe, and Y. Takano, *J. Phys. C* **9**, 1665 (1976).

[31] J. Wilks, **The Properties of Liquid and Solid Helium** Chap. 15 (Oxford Univ. Press, London, 1967).

[32] P.C. Hammel and R.C. Richardson, *Phys. Rev. Lett.* **52**, 1441 (1984).

[33] R.C. Richardson, *Physica* **126B**, 298 (1984).

[34] P.C. Hammel, M.L. Roukes, Y. Hu, T.J. Gramila, T. Mamiya, and R.C. Richardson, *Phys. Rev. Lett.* **51**, 2124 (1983).

[35] O. Gonen, P.L. Kuhns, C. Zuo, and J.S. Waugh, *J. Mag. Res.* **81**, 491 (1989).

[36] N.S. Sullivan, *J. Low Temp. Phys.* **22**, 313 (1976).

[37] A. Schuhl, S. Maegawa, M.W. Meisel, and M. Chapellier, *Phys. Rev. B* **36**, 6811 (1987).

[38] P.C. Hammel, P.L.Kuhns, O. Gonen, and J.S. Waugh, *Phys. Rev. B* **34**, 6543 (1986).

[39] L.J. Friedman, T.J. Gramila, and R.C. Richardson, *J. Low Temp. Phys.* **55**, 83 (1984).

[40] F.W. Van Keuls, T.J. Gramila, L.J. Friedman, and R.C. Richardson, *Physica B* **165 & 166**, 717 (1990).

[41] R. Ling, E.R. Dobbs, and J. Saunders, *Phys. Rev. B* **33**, 629 (1986).

[42] D.O. Edwards, J.D. Feder, W.J. Gully, G.G. Ihas, J. Landau, and K.A. Muething, in *Physics at Ultralow Temperatures*, Proceedings of the 1977 Hakone International Symposium, T. Sugawara *et al.*, eds. (Physical Society of Japan, Tokyo, 1978).

[43] O. Avenel, P.M. Berglund, and E. Varoquaux (unpublished) cited in ref [42].

[44] N.S. Sullivan, M. Rall, and D. Zhou, *Proc. Quant. Fluids and Solids 1989*, G.G. Ihas and Y. Takano, eds., AIP Conf. Proc. **194**, 403 (1989).

[45] P.M. Anderson, N.S. Sullivan, M. Rall, and J.P. Brison, *Physica B* **169**, 453 (1991).

[46] P.M. Anderson, N.S. Sullivan, B. Andraka, J.S. Xia, and E.D. Adams, *Phys. Lett. A* **172** 85 (1992).

[47] L. Pollack, E.N. Smith, J.M. Parpia, and R.C. Richardson, *J. Low Temp. Phys.* **87** 753 (1992).

[48] F. Pobell, **Matter and Methods at Low Temperatures** (Springer-Verlag, 1992).

[49] J.S. Waugh, O. Gonen, and P. Kuhns, *J. Chem. Phys.* **86**, 3816 (1986).

[50] E.B. Genio, J. Xu, T. Lang, G.G. Ihas, and N.S. Sullivan, *J. Low Temp. Phys.* **101**, 611 (1995).

[51] E.B. Genio, J. Xu, N.S. Sullivan, and G.G. Ihas, *Czech. J. Phys.* **46**, 219 (1996).

[52] Kiho Kim, J.R. Bodart, and N.S. Sullivan, *J. Mag. Res.* **118**, 28 (1996).

BIOGRAPHICAL SKETCH

Edgar B. Genio was born in Naga City, Philippines on April 15, 1964. After receiving his elementary and high school education, he studied physics at the National Institute of Physics, University of the Philippines in Quezon City, Philippines.

After teaching for a year, he went to the University of Florida in Gainesville for graduate studies in Physics. He studied under Prof. Neil Sullivan and joined his Low Temperature NMR research group.

I certify that I have read this study and that in my opinion it conforms to acceptable standards of scholarly presentation and is fully adequate, in scope and quality, as a dissertation for the degree of Doctor of Philosophy.

N S Sullivan

Neil S. Sullivan, Chairman
Professor of Physics

I certify that I have read this study and that in my opinion it conforms to acceptable standards of scholarly presentation and is fully adequate, in scope and quality, as a dissertation for the degree of Doctor of Philosophy.

Gary G. Ihas

Gary G. Ihas
Professor of Physics

I certify that I have read this study and that in my opinion it conforms to acceptable standards of scholarly presentation and is fully adequate, in scope and quality, as a dissertation for the degree of Doctor of Philosophy.

E. Dwight Adams

E. Dwight Adams
Professor of Physics

I certify that I have read this study and that in my opinion it conforms to acceptable standards of scholarly presentation and is fully adequate, in scope and quality, as a dissertation for the degree of Doctor of Philosophy.

David Tanner
Professor of Physics

I certify that I have read this study and that in my opinion it conforms to acceptable standards of scholarly presentation and is fully adequate, in scope and quality, as a dissertation for the degree of Doctor of Philosophy.

Peter Hirschfeld
Associate Professor of Physics

I certify that I have read this study and that in my opinion it conforms to acceptable standards of scholarly presentation and is fully adequate, in scope and quality, as a dissertation for the degree of Doctor of Philosophy.

Wallace S. Brey

Wallace S. Brey
Professor of Chemistry

This dissertation was submitted to the Graduate Faculty of the Department of Physics in the College of Liberal Arts and Sciences and to the Graduate School and was accepted as partial fulfillment of the requirements for the degree of Doctor of Philosophy.

May 1997

Dean, Graduate School